Universiteit Utrecht

Opleiding Natuur- en Sterrenkunde

Analyzing time evolution of a tidal inlet due to nonlinear tides, sea level rise and waves with an idealised model

Bachelor Thesis

Philippe Frankemölle

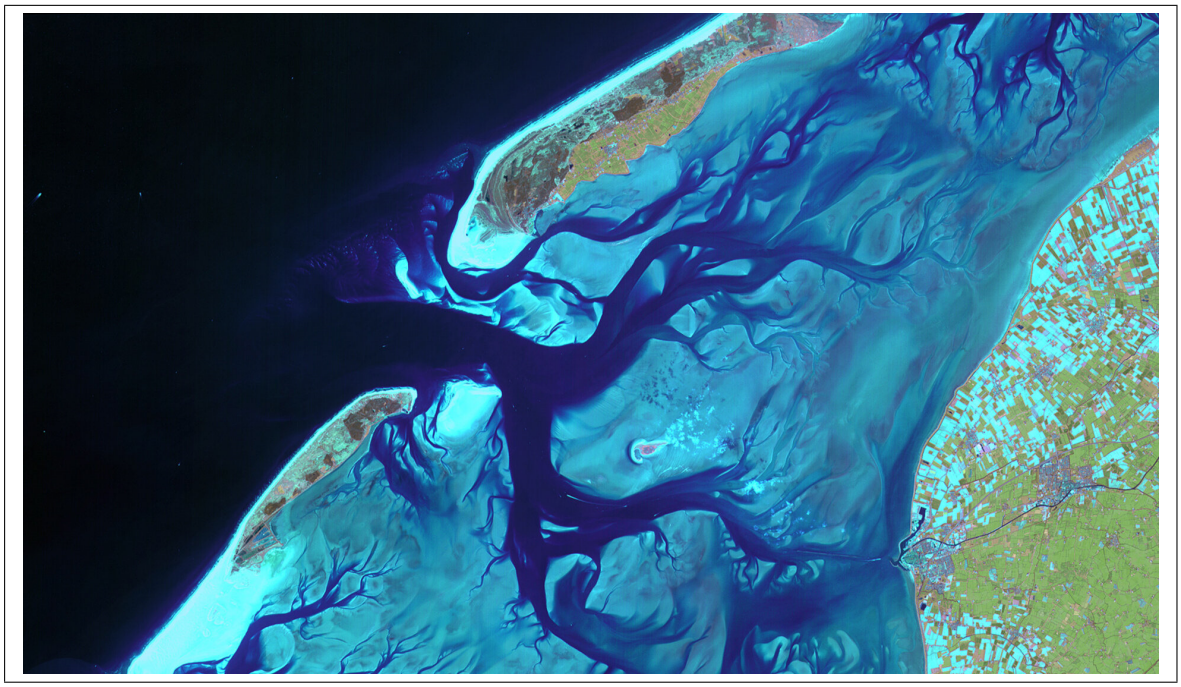

Supervisor:

Prof. Dr. H.E. (Huib) de Swart
IMAU

June 12, 2020

Abstract

A tidal inlet is a connection between the ocean and a basin behind the shoreline, in which water motion is dominated by tides. Such basins evolve over time due to asymmetries in tidal currents, waves and sea level rise. The primary objective of this research was to establish the presence of stable morphodynamic equilibria exist for tidal inlet systems. Other goals were finding the dominant hydrodynamic processes governing net sand transport and studying the response of the basin to sea level rise and waves. This has been done by calculating approximate solutions to one-dimensional nonlinear shallow water equations, and coupling them to simplified expressions for sand transport, as well as for evolution of length and depth. It is found that tidal currents can create stable equilibria, but not for basins with dimensions that resemble those on the Holland coast, with lengths less than 100 km. In particular, it is found that for smaller sized basins, infilling by the tidal current alone is too weak to compensate for the creation of accommodation space by current-day sea level rise. The simulations are in line with research on the Holocene evolution of the Holland coast. The Wadden Sea has not closed during this time, since the transport due to tides and waves was sufficient to compete with sea level rise. However, with projections of higher sea level rise in the near future, the Wadden Sea is at risk of drowning.

The picture on the front page shows a satellite image made by the European Space Agency (ESA) of part of the Dutch Wadden Sea. This sea is an official UNESCO World Heritage Site, because of its strong response to tides. The Wadden Sea is connected to the ocean through the gaps between the Frisian Islands. This picture showcases the Vlie inlet, located between the islands Vlieland and Terschelling. This entrance from the ocean to the Wadden Sea is an example of a tidal inlet.

Contents

1 Introduction

The title of this thesis perfectly summarises the research, but perhaps it may be a bit too much to digest in one go. So before diving into the specifics, let us take the time to decompose this sentence and find out its meaning step by step. The first course of action is explaining what a tidal inlet entails, why they are the important and how they come into existence. From there the step is made to nonlinear tides, sea level rise and waves and their connection with time evolution of those inlets.

1.1 Background on tidal inlets

A clear definition of a tidal inlet is given in the book Beaches and Coasts (*Davis Jr and FitzGerald*, 2009):

"*A tidal inlet is defined as an opening in the shore through which water penetrates the land thereby proving a connection between the ocean and bays, lagoons, and marsh and tidal creek systems. The main channel of a tidal inlet is maintained by tidal currents.*"

A tidal inlet can be created in several ways, two from which will be elaborated on following Beaches and Coasts. These inlets mostly occur because of a combination of a weakened shore due to erosion and a heavy storm. The storm surges in the backbarrier flow across the shore and creates an opening in the fragile barrier coastline. If tidal flow is able to maintain this opening, a tidal inlet is created. Another origin of tidal inlets is drowned river valleys. Imagine a river flowing to the ocean when the sea level is low. Due to melting ice the sea level suddenly rises swiftly and this river (valley) starts to drown. Estuaries form in the old river valley, because of the mixing of freshwater and saltwater from the river and ocean. Due to sediment deposits barrier islands can be formed, which narrow the entrance to the estuary. This eventually ends up becoming a tidal inlet. The title page shows an example of a tidal inlet: the gap between the barrier islands Texel and Vlieland. Together with the other Frisian islands, Texel and Vlieland shield the backbarrier system (the Wadden Sea) from the North Sea. The Wadden Sea is extremely tide dominated as large parts of it fall completely dry during ebb. Typical lengths for a tidal basin range from 10 to 100 km, where 100 km is considered very long. A typical depth would be that of $\sim$ 10 m.

1.2 Evolution of a tidal inlet

So apparently tides are important for tidal inlets. But why are 'nonlinear tides' important enough to be mentioned in the title? In an ideal world the currents in the ocean close to the inlet are described as a pure sinusoidal signal. When entering the tidal basin the signal is influenced by nonlinear terms in the equations of motion that govern tides. Because of this, the current is divided into a principal tide (M2), a first overtide (M4), and a residual tide (M0). The interactions between M2-M4 and M2-M0 lead to asymmetries in the tide. Such asymmetries can be observed in Figure 1.

Sand transport is induced by a current and in the case of a tidal inlet this has to be a tidal

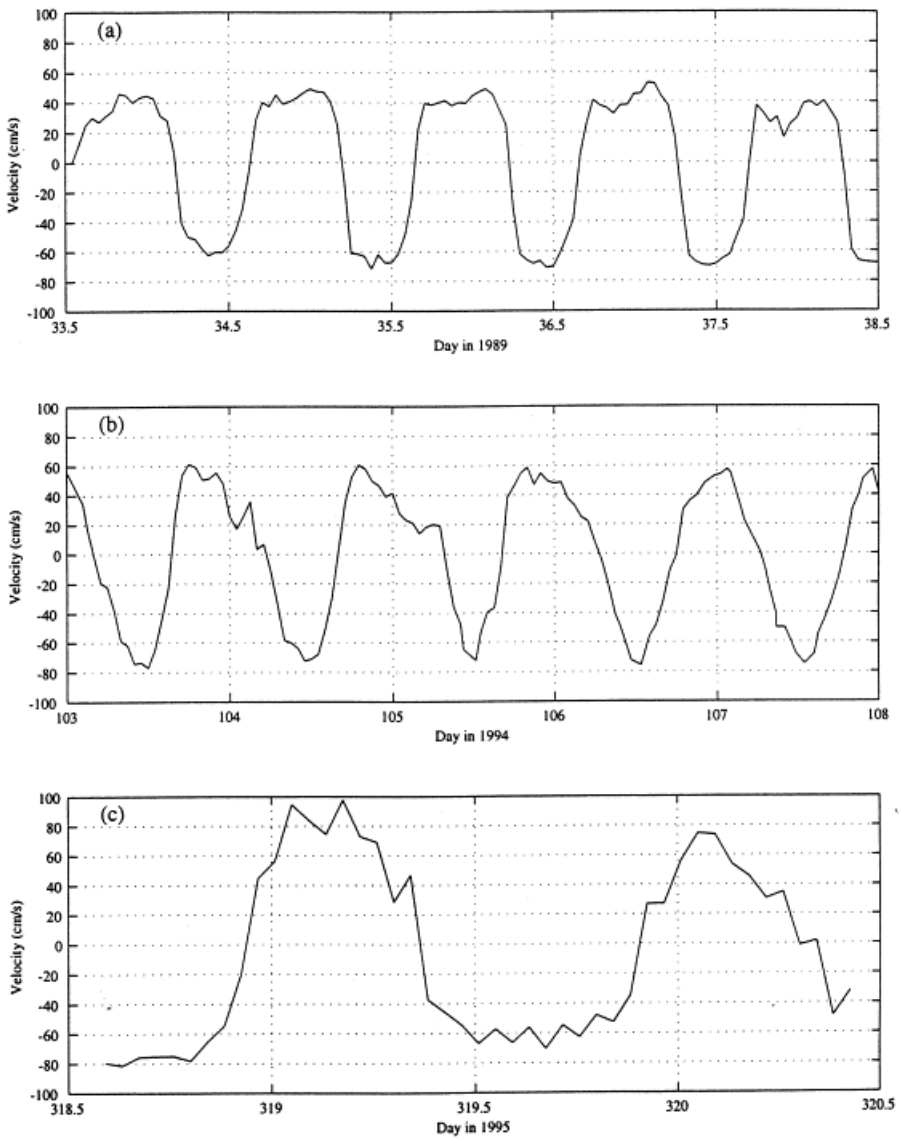

Figure 1: Time series of inlet currents measured at (a) Swan River estuary: ebb-dominant; (b) Peel–Harvey estuary: ebb-dominant; and, (c) Wilson inlet: flood-dominant. Positive and negative velocities indicate flood and ebb velocities, respectively. Figure and caption are directly taken from a paper about tidal inlet velocity asymmetry in diurnal regimes (*Ranasinghe and Pattiaratchi*, 2000).

current. When a tide is symmetric, the magnitude and duration of ebb and flood will be the same and there will be no net transport during the period of one tide. If the tide is asymmetric however, the magnitude and/or duration of either ebb or flood is longer and there will be a tidally averaged sand transport. Sand transport is not linearly dependant on velocity, meaning that even if the mean velocity is zero, the transport does not have to be. So nonlinear tides create asymmetries, that allow tidal currents to induce sand transport, which in turn changes the size of a tidal inlet.

Theory and observations indicate that sea level rise and sand transport due to waves respectively causes lengthening/deepening and closure of the tidal basin (*Beets et al.*, 2000; *Davis Jr and FitzGerald*, 2009; *Escoffier*, 1940). The competition between tidal currents, sea level rise and waves determines the evolution of the basin. Beets states that waterways along the Holland coast closed due to decreasing sea level rise, whereas farther to the north/south they managed to stay open due to strong tidal currents.

The evolution of tidal inlets is more than just an intriguing physical concept; it can alter the course of history. Many Dutch people have learned in school about the rapid growth and enormous wealth of Amsterdam during the seventeenth century. They managed to prosper because the former 'market of the world', Antwerp, had fallen to the Spanish and the Belgian merchants fled to Amsterdam. Both large cities relied on its harbors and connections to the sea. But before Antwerp became big in the fifteenth century, North-West Europe had another economic capital: Bruges.

In 1134 a heavy storm broke through the Flemmish coast, creating the Zwin, a tidal inlet system. This gave the city of Bruges direct access to the ocean, which lead them to canalise the city. This allowed them to expand their markets and become one of the most influential medieval port cities (*Murray*, 2005). Bruges reached its golden age in the fourteenth century because of its thriving harbors. The Zwin was unfortunately sanding in, ultimately causing the waterway to become unusable in the fifteenth century. Due to the loss of direct access to the ocean and other political factors, Antwerp eventually took over Bruges' economic cornerstone position. If it were not for the tidal inlet, (history-)rich Bruges would probably not be a UNESCO World Heritage Site today.

1.3 The topic of the research

To summarise the last paragraph: nonlinear processes cause asymmetries, which in turn induce transport of sand. The size and shape of the inlet influence the current. The current decides the magnitude and sign of the transport. And of course are the size and shape of the basin altered by erosion and sand deposition. And thus there is a feedback loop, which determines the evolution of a tidal inlet over time.

The primary aim of the research is finding out if a tidal inlet system is capable of reaching a stable equilibrium. The concepts of stability closely follow the hypothesis formulated by Escoffier in his article on the stability of tidal inlets (*Escoffier*, 1940), which is also used in similar studies such as (*Reef et al.*, 2020), which discusses the effects of different basin

geometries. The secondary goal is to determine the dominant hydrodynamic processes that cause sand transport. The last research goal is to test the response of the model to multiple scenario's of sea level rise and sand transport due to waves in order to find critical values for sea level rise in order to maintain an inlet. This is inspired by an article on the Holocene evolution of the Dutch and Belgian coast as a function of relative sea level rise and sediment supply (*Beets et al.*, 2000) and more recent research on the effect of relative sea level rise on the Wadden Sea (*Lodder et al.*, 2019). This research, among others, predicts the system to drown should the sea level rise increase above a critical rate.

To achieve all this, a simplified one-dimensional model of a tidal inlet is created, using various mathematical tools and some basic programming, with a similar approach as the articles reviewed by de Swart on morphodynamics of tidal inlet systems (*De Swart and Zimmerman*, 2009). The big difference between this study and existing studies is the simplified expression for sand transport. Here, it only depends on the transport at the entrance of the basin, without accounting for critical velocity values necessary to initiate sand transport. This method makes up for its crudeness by significantly increasing the time over which a basin can be evaluated.

2 Theory

The hypothesis formulated in the introduction is that due to nonlinear terms in the governing equations of water motion, asymmetries in the flow will appear. Then, because of these tidal asymmetries, import or export of sand will occur and the size of the basin will change over time.

Section 2.1 will describe and sketch the domain of the model. In section 2.2, proper boundary conditions and scaling relations are used to make the governing (nonlinear) equations dimensionless. Section 2.3 will discuss a method called Lorentz' linearisation, which is used to linearise a quadratic stress term. Next, by applying perturbation analysis, two sets of linear differential equations can be derived. Those will be solved in section 2.4, giving expressions for tidal asymmetries. In section 2.5 a relation between phase differences, sand transport and evolution of the basin will be found, using conservation of volume. Lastly, everything will come together in section 2.6, where the structure of the script written for this research is explained.

2.1 Sketch of the domain

Before committing entirely to mathematical derivations it is important to visualise the domain. In the idealised model that will be worked with, the tidal inlet is a perfectly rectangular box connected to the ocean at coordinate $x = 0$. The inlet has a length L_b, a mean depth H and a width b. The latter will have no influence in the one dimensional problem that is solved in this thesis, but is included for completeness. The water depth deviates from the mean depth with η. The domain is sketched in Figure 2.

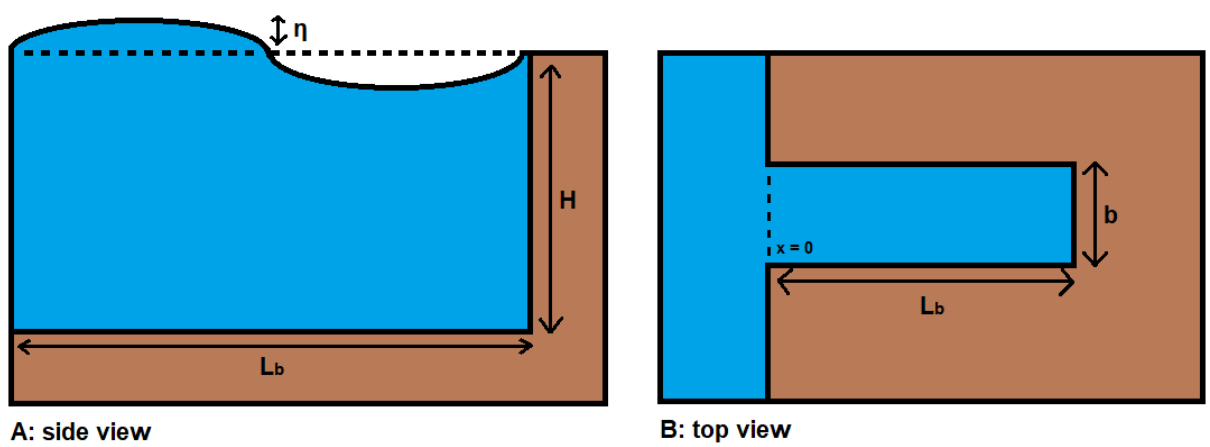

Figure 2: Side view (**A**) and top view(**B**) of the tidal inlet. Here, L_b, H and b respectively indicate the length, mean depth and width of the inlet and η is the height deviation from the mean depth.

2.2 Equations for tidal motion

It is assumed that the water motion in the tidal basin is governed by the one-dimensional shallow water equations:

$$\frac{\partial u}{\partial t} + u\frac{\partial u}{\partial x} = -g\frac{\partial \eta}{\partial x} - \frac{c_d|u|u}{H+\eta}, \tag{1}$$

$$\frac{\partial \eta}{\partial t} + \frac{\partial}{\partial x}([H+\eta]u) = 0, \tag{2}$$

with boundary conditions

$$\eta = Z\cos(\omega t); \quad \text{at } x = 0, \tag{3}$$

$$u = 0; \quad \text{at } x = L_b. \tag{4}$$

Here, x is the coordinate along the channel, t is the time, u is the velocity in the x-direction, H is the mean depth of the basin, η is the height deviation from the mean depth, g is the gravitational acceleration and c_d is a drag coefficient. The first boundary condition states that at the entrance of the basin the height deviation always acts as a pure sinusoidal wave with amplitude Z and angular frequency ω. The second condition implies that there can be no perpendicular motion at the end of the basin. Solving this system without making some prior adjustments will prove to be difficult, as it is nonlinear and thus has no analytical solutions. The goal will be to find approximate solutions by assuming the nonlinear terms to be small with respect to linear terms.

The first step is writing them down in dimensionless form. Scaling relations have to be established in order to do so. Judging from the first boundary condition η can be scaled with the amplitude of the incoming wave Z. The inverse of the angular frequency ω has the dimensions of time and makes for a suitable candidate to scale the time t. The coordinate x, can be scaled with the frictionless wavelength of the tide, which goes as $L_t = \sqrt{gH}\omega^{-1}$, disregarding a factor 2π. Using these scales it is possible to derive the last scaling relation, for velocity u. Using the assumption that nonlinear terms are small with respect to linear terms it can be argued that $[\frac{\partial u}{\partial t}] \sim [g\frac{\partial \eta}{\partial x}]$. Inserting the already known scaling relations results in a scale $U \sim Zg^{1/2}H^{-1/2}$ for the velocity u.

The resulting scaling equations are thus:

$$\begin{aligned} u &= \sqrt{\frac{g}{H}}Z\tilde{u}, \\ \eta &= Z\tilde{\eta}, \\ t &= \omega^{-1}\tilde{t}, \\ x &= \frac{\sqrt{gH}}{\omega}\tilde{x}, \end{aligned} \tag{5}$$

where the symbols with tildes are dimensionless. Substituting the scaling relations into equations (1) to (4) and applying appropriate divisions leads to the following dimensionless system:

$$\frac{\partial \tilde{u}}{\partial \tilde{t}} + \epsilon \tilde{u} \frac{\partial \tilde{u}}{\partial \tilde{x}} = -\frac{\partial \tilde{\eta}}{\partial \tilde{x}} - \alpha \frac{c_d |\tilde{u}| \tilde{u}}{1 + \epsilon \tilde{\eta}}, \tag{6}$$

$$\frac{\partial \tilde{\eta}}{\partial \tilde{t}} + \frac{\partial}{\partial \tilde{x}}([1 + \epsilon \tilde{\eta}]\tilde{u}) = 0, \tag{7}$$

with boundary conditions

$$\tilde{\eta} = \cos(\tilde{t}); \quad \text{at } \tilde{x} = 0, \tag{8}$$

$$\tilde{u} = 0; \quad \text{at } \tilde{x} = \ell. \tag{9}$$

Three new parameters have been introduced in these dimensionless equations: α, ℓ and ϵ. They are given by:

$$\begin{aligned} \alpha &= Z \frac{g^{1/2}}{\omega H^{3/2}}, \\ \ell &= \frac{L_b}{L_t}, \\ \epsilon &= \frac{U}{\sqrt{gH}} = \frac{Z}{H}. \end{aligned} \tag{10}$$

In equation (10), ϵ is called the Froude number, the importance of which will become apparent in section 2.4 when perturbation analysis comes into play. The assumption has been used that all nonlinear terms should be small with respect to linear terms. While ϵ is a small number, α is not. This means that the quadratic friction term in equation (6) does not satisfy the assumption. In order to bypass this conundrum and find approximate solutions, the next step will be to linearise the stress term.

2.3 Lorentz' linearisation

From this point onward the dimensionless equations introduced in the former section will be written without tildes for the sake of legibility. In order to linearise the friction term, a similar method will be used as by Lorentz during calculations for the Zuiderzee Works, using energy arguments(*Lorentz*, 1926). The goal here is to find an expression for the linear friction coefficient λ:

$$\alpha c_d |u| u \to \lambda u. \tag{11}$$

In order for this to hold, the requirement is added that both quadratic and linear stress induce the same mean energy dissipation over a tidal period. This yields

$$\alpha \int_0^\ell \frac{1}{2\pi} \int_0^{2\pi} c_d |u| u^2 dt dx = \int_0^\ell \frac{1}{2\pi} \int_0^{2\pi} \lambda u^2 dt dx. \tag{12}$$

The integration takes place from 0 to ℓ, which is the entire scaled length of the basin. By rearranging the former equation a little and introducing $\langle ... \rangle = \frac{1}{2\pi} \int_0^{2\pi} ... \, dt$, an expression for the linear friction coefficient can be obtained:

$$\lambda = \alpha c_d \frac{\int_0^\ell \langle |u|^3 \rangle dx}{\int_0^\ell \langle |u|^2 \rangle dx}. \tag{13}$$

There is one snake in the grass that a keen reader may have already noticed. We need this linearised friction term in order to compute our velocity, but λ itself depends on the velocity. Section 2.6 will further expand on how to iteratively find a value for λ.

2.4 Construction of approximate solutions

The next big step is to take the set of non-linear differential equations and simplify it to two sets of linear differential equations. This will be done by introducing perturbation analysis. The ansatz is that flow u and height deviation η can be described as a dominant term with a small perturbation on top of it. This can be written as

$$u = u_0 + \epsilon u_1 + O(\epsilon^2), \tag{14}$$

$$\eta = \eta_0 + \epsilon \eta_1 + O(\epsilon^2). \tag{15}$$

For this to hold, the assumption is made that the Froude number $\epsilon \ll 1$. Judging from the last expression in (10), this means that the height deviation should be way smaller than the depth of the tidal inlet. Before substituting these expressions in the shallow water equations, it is necessary to simplify the friction term (including the denominator). For this a first order Taylor approximation will be used, which transforms the last term to: $\lambda u_0(1 - \epsilon\eta_0) + \lambda u_1$. After using the ansatz on the shallow water equations and separating the zeroth- and first-order terms (all higher-order terms are considered negligible) two sets of linear differential equations appear. The zeroth-order system is:

$$\frac{\partial u_0}{\partial t} + \frac{\partial \eta_0}{\partial x} + \lambda u_0 = 0, \tag{16}$$

$$\frac{\partial \eta_0}{\partial t} + \frac{\partial u_0}{\partial x} = 0, \tag{17}$$

with boundary conditions

$$\eta_0 = \cos(t); \quad \text{at } \ x = 0, \tag{18}$$

$$u_0 = 0; \quad \text{at } \ x = \ell. \tag{19}$$

The first-order system reads:

$$\frac{\partial u_1}{\partial t} + \frac{\partial \eta_1}{\partial x} + \lambda u_1 = -u_0 \frac{\partial u_0}{\partial x} + \lambda u_0 \eta_0, \tag{20}$$

$$\frac{\partial \eta_1}{\partial t} + \frac{\partial u_1}{\partial x} = -\frac{\partial}{\partial x}(u_0 \eta_0), \tag{21}$$

with boundary conditions

$$\eta_1 = 0; \quad \text{at } \ x = 0, \tag{22}$$

$$u_1 = 0; \quad \text{at } \ x = \ell. \tag{23}$$

2.4.1 Zeroth-order system

It is apparent that, in order to solve the first-order system, expressions for the dominant flow, u_0 and η_0, are required. Those can be obtained from the zeroth-order system. By taking the time derivative of (16) and substituting in (17), the following partial differential equation can be obtained:

$$\frac{\partial^2 u_0}{\partial x^2} = \frac{\partial^2 u_0}{\partial t^2} + \lambda \frac{\partial u_0}{\partial t}. \tag{24}$$

By combining equation (16) and (18), the first boundary condition can be expressed in terms of u_0. The boundary condition now yields

$$\frac{\partial u_0}{\partial x} = \sin(t); \quad \text{at } \ x = 0. \tag{25}$$

Now solutions are found by using separation of variables. Because the equations are linear and have constant coefficients, the solutions will have an exponential form. The solutions that are sought are non-transient, meaning they purely depend on the forcing and not on initial conditions. Hence they oscillate with the same angular frequency as the imposed tide at $x = 0$. With the knowledge that our velocity must be real the ansatz for the solution of u_0 can be written as

$$u_0 = \Re\{\hat{u}_0(x)\ e^{-it}\}. \tag{26}$$

Filling in the ansatz leads to a simple homogeneous second-order linear differential equation:

$$\frac{d^2 \hat{u}_0}{dx^2} + k_0^2 \hat{u}_0 = 0. \tag{27}$$

In this equation k_0 is the complex wave number of the dominant flow, which is given by $\sqrt{1 + i\lambda}$. This differential equation takes the form of a harmonic oscillator, hence it has the standard solution:

$$\hat{u}_0 = Ae^{ik_0 x} + Be^{-ik_0 x}. \tag{28}$$

The boundary conditions yield expressions for integration constants A and B. A detailed calculation can be found in the appendix. The solution is:

$$\hat{u}_0 = -i \frac{\sin(k_0(x - \ell))}{\cos(k_0 \ell)}. \tag{29}$$

An ansatz can be given for η_0, based on the same reasoning as for u_0:

$$\eta_0 = \Re\{\hat{u}_0(x)\ e^{-it}\}. \tag{30}$$

Combining this with equation (17) and the expression for u_0, this yields the following expression for the complex amplitude of η_0:

$$\hat{\eta}_0 = \frac{\cos(k_0(x - \ell))}{\cos(k_0 \ell)}. \tag{31}$$

2.4.2 First-order system

On the right hand side of the first equation, the advection term ($-u_0\partial_x u_0$) and the depth-dependent friction term ($\lambda u_0\eta_0$) appear. In the second equation the divergence of the excess mass flux ($-\partial_x[u_0\eta_0]$) appears. These will be referred to as respectively ADV, DDF and EMF.

The course of action now is to solve this set of equations for each term independently. This is a valid strategy, as the solutions of these linear equations can all be added using a superposition argument. The following part will describe the general method used to find solutions for every term. The specific calculations per are given in the appendix.

First, equation (26) is slightly rewritten:

$$u_0 = \frac{1}{2}\hat{u}_{01}e^{-it} + \frac{1}{2}\hat{u}_{01}^{*}e^{it}. \tag{32}$$

Likewise, the sea surface elevations of the zeroth-order system are written as

$$\eta_0 = \frac{1}{2}\hat{\eta}_{01}e^{-it} + \frac{1}{2}\hat{\eta}_{01}^{*}e^{it}. \tag{33}$$

Note that the notation of $\hat{u}_0$ has been altered slightly to $\hat{u}_{01}$. The first index denotes which order the term is and the second term which tidal harmonic it corresponds to. The first tidal harmonic is the fundamental frequency, the lowest frequency sinusoidal; in this case that is ω. The second tidal harmonic is twice the first harmonic (2ω), the third harmonic is thrice the first harmonic (3ω), etc. The zeroth harmonic corresponds to a frequency of 0 Hz.

Expressing the external forcing terms (ADV, DDF, EMF) of equations (20) and (21) in terms of our rewritten expressions gives terms of solely zeroth and second tidal harmonic. Since the solutions are again non-transient, it stands to reason that the perturbations of velocity and height deviation are expressed as

$$u_1 = \bar{u}_{10} + \frac{1}{2}\hat{u}_{12}e^{-2it} + \frac{1}{2}\hat{u}_{12}^{*}e^{2it} \tag{34}$$

and

$$\eta_1 = \bar{\eta}_{10} + \frac{1}{2}\hat{\eta}_{12}e^{-2it} + \frac{1}{2}\hat{\eta}_{12}^{*}e^{2it}. \tag{35}$$

The zeroth harmonic terms are called the (tidal) residual and the second harmonic terms are called the (first) overtide. Next, equations (32)-(35) are substituted into equations (19) and (20) for each independent process. Then the equations can be split into two groups: zeroth harmonic and second harmonic. Hence every process then gets two sets of linear differential equations, one set for the residual term and one set for the overtide term.

These sets can be solved in a similar fashion as done with the zeroth-order problem. The calculation of the residual terms is straightforward. Integrating the continuity equation from $x' = x$ to $x' = \ell$ and applying the boundary conditions for u_0 and u_1 at $x = \ell$ leads to

$$\bar{u}_{10} = -\frac{1}{4}\hat{u_0}\hat{\eta_0}^{*} - \frac{1}{4}\hat{u_0}^{*}\hat{\eta_0}. \tag{36}$$

This can be interpreted as a return flow, compensating for the net mass transport $u_0\eta_0$ towards the land caused by the tidal wave.

The differential equations for the overtide are slightly harder to solve, since they become forced harmonic oscillators. Those equations look like

$$\frac{d^2\hat{u}_{12}}{dx^2} + k_1^2\hat{u}_{12} = f(x), \tag{37}$$

with $f(x)$ some function composed of $\hat{u}_{01}$ and $\hat{\eta}_{01}$. Using the variation of constants technique gives solutions of the form

$$\hat{u}_{12} = A(x)e^{ik_1x} + B(x)e^{-ik_1x}, \tag{38}$$

where k_1 is the wave number corresponding to the overtide terms, which is given by $\sqrt{4+2i\lambda}$. The final expressions (evaluated at the entrance of the basin) become:

$$\bar{u}_{10,ADV} = 0 \tag{39}$$

$$\bar{u}_{10,DDF} = 0 \tag{40}$$

$$\bar{u}_{10,EMF} = -\frac{1}{4}\hat{u}_0\hat{\eta}_0{}^* - \frac{1}{4}\hat{u}_0{}^*\hat{\eta}_0 \tag{41}$$

$$\hat{u}_{12,ADV} = \frac{i}{4k_1\cos^2(k_0\ell)}\left(\frac{\sin((k_1-2k_0)\ell)}{k_1-2k_0} - \frac{\sin((k_1+2k_0)\ell)}{k_1+2k_0}\right)\left(\cos(k_1\ell) + \frac{\sin^2(k_1\ell)}{\cos(k_1\ell)}\right) \tag{42}$$

$$\hat{u}_{12,DDF} = -\frac{i\lambda}{4k_0k_1\cos^2(k_0\ell)}\left(\frac{\sin((2k_0+k_1)\ell)}{2k_0+k_1} + \frac{\sin((2k_0-k_1)\ell)}{2k_0-k_1}\right)\left(\cos(k_1\ell) + \frac{\sin^2(k_1\ell)}{\cos(k_1\ell)}\right) \tag{43}$$

$$\hat{u}_{12,EMF} = -\frac{ik_0}{2k_1\cos^2(k_0\ell)}\left(\frac{\sin((k_1+2k_0)\ell)}{k_1+2k_0} - \frac{\sin((k_1-2k_0)\ell)}{k_1-2k_0}\right)\left(\cos(k_1\ell) + \frac{\sin^2(k_1\ell)}{\cos(k_1\ell)}\right) - \frac{ik_0\cos(2k_0\ell)}{2k_1\cos^2(k_0\ell)\cos(k_1\ell)}\sin(k_1\ell) \tag{44}$$

So far, expressions have been derived for the velocity in terms of complex amplitudes. Naturally, those complex amplitudes can be rewritten in polar form, in terms of its modulus and its argument. Hence, all complex velocities can be rewritten as

$$\hat{u}_{mn} = |\hat{u}_{mn}|e^{i\,\phi_{mn}}. \tag{45}$$

So a component of the velocity (taking time into account) will look like

$$u_{mn} = \Re\{|\hat{u}_{mn}|e^{i(\phi_{mn}-nt)}\} = |\hat{u}_{mn}|\cos(nt-\phi_{mn}). \tag{46}$$

The importance of those phase shifts, or more precisely phase differences between two velocity terms, will be elaborated on in the next section.

2.5 Sand transport and time evolution

So far, an approximate solution for the velocity has been derived. This subsection will connect the velocity to sand transport, which ultimately leads to an expression for time evolution of the basin. From observations and theoretical consideration it can be argued that the sand transport rate q is proportional to the velocity cubed: $q \propto u^3$ (*Colling et al.*, 1999). Normally, one could also take into account a certain threshold velocity necessary to start sand transport; for the sake of simplicity this is ignored; it is thus assumed that during large parts of the tidal cycle the actual velocity is much larger than the critical velocity for erosion. The expression used in this research is given by

$$q = \gamma u^3. \tag{47}$$

Here, γ denotes a constant with the units $\mathrm{s^2m^{-1}}$. Hence the units of q themselves is $\mathrm{m^2s^{-1}}$, which is logical given that the model has no depth. Such an expression provides the transport rate for each time t. Because the point of interest lies in time evolution over periods of thousands of years, calculating the exact transport during every second would be quite counterproductive. So the interest is in $\langle q \rangle$, the net transport rate over one tidal period. This is written as

$$\langle q \rangle = \frac{\gamma}{2\pi} \int_0^{2\pi/\omega} u^3 dt. \tag{48}$$

In order to do this, it is assumed that the size of the basin cannot fluctuate drastically during a tidal period, as that would of course influence the flow. The model that has been used so far is dimensionless, so of course $\langle q \rangle$ has to be rewritten in its dimensionless counterpart, using the same scaling relations as before. This means that $\langle q \rangle = \gamma U^3 \langle \tilde{q} \rangle$. Thus the dimensionless net sediment transport becomes

$$\langle q \rangle = \frac{1}{2\pi} \int_0^{2\pi} u^3 dt, \tag{49}$$

where the tilde is again dropped for convenience. The total velocity takes the form

$$\begin{aligned} u =& |\hat{u}_{01}| \cos(t - \phi_{01}) + \epsilon(\bar{u}_{10,EMF} + |\hat{u}_{12,EMF}| \cos(2t - \phi_{12,EMF}) \\ &+ |\hat{u}_{12,ADV}| \cos(2t - \phi_{12,ADV}) + |\hat{u}_{12,DDF}| \cos(2t - \phi_{12,DDF})). \end{aligned} \tag{50}$$

Evidently, it is quite the hassle to calculate every term of $\langle q \rangle$. One of the main spearheads of this research is that the phase difference between tidal terms is the decisive factor for sand transport. To illustrate this point $\langle q \rangle$ will be calculated as following:

$$\langle q \rangle = \frac{1}{2\pi} \int_0^{2\pi} (|\hat{u}_{01}| \cos(t - \phi_{01}) + \epsilon \bar{u}_{10} + \epsilon |\hat{u}_{12}| \cos(2t - \phi_{12}))^3 dt. \tag{51}$$

Many cross terms drop because of symmetry arguments, what remains is

$$\langle q \rangle = \frac{3}{4}\epsilon |\hat{u}_{01}|^2 |\hat{u}_{12}| \cos(\Delta\psi) + \frac{3}{2}\epsilon |\hat{u}_{01}|^2 \bar{u}_{10} + \frac{3}{2}\epsilon^3 \bar{u}_{10} |\hat{u}_{12}|^2 + \epsilon^3 \bar{u}_{10}^3, \tag{52}$$

where $\Delta\psi$ is defined as $\phi_{12} - 2\phi_{01}$. The first dominant term of the transport ($O(\epsilon)$) depends on this phase difference. So this equation confirms that the phase difference between the

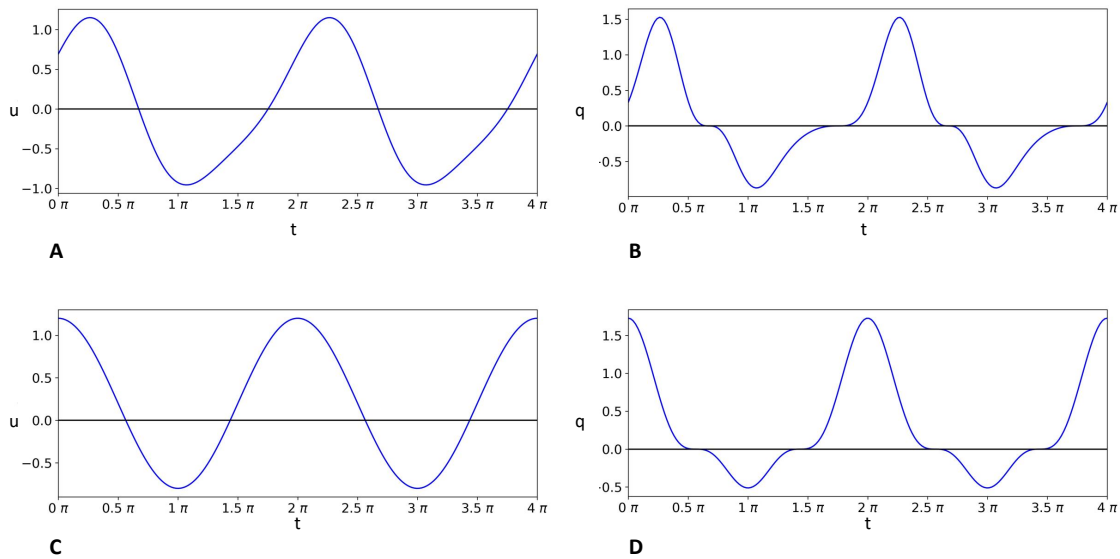

Figure 3: Plots showing a M2-tide with asymmetries due to a M4-term (**A**) and a M0-term (**C**) during two tidal periods. **B** and **D** show their respective transport q(t) The phase difference between the M2- and M4-tide is 0.3π. Both cases feature a flood dominated basin.

M4-tide and the M2-tide is responsible for sand transport. The second dominant term shows the interaction between the M0- and M2-tide. Figure 3 visualises what the flow and transport can look like during two tidal periods due to first overtide and residual flow. Both clearly induce a net transport, which explain the existence of the two dominant terms for sand transport. When splitting the M4-tide in three different components (ADV, DDF, EMF), some additional terms appear due to phase differences between those terms. These net sand transport terms are only of the order ϵ^3.

Two major simplifications with respect to erosion and deposition of sand within the basin are made in this research.

1. Erosion and deposition are related to net transport at the entrance of the basin.
2. After entering or exiting the basin, all sand will instantaneously be spread uniformly over part of the length and/or part of the depth.

The last step is relating the sand transport to actual time evolution. The starting point for this will be the conservation of volume. In other words: if a certain volume of sand is transported into the basin, the same volume of water has to exit. Since the basin will always remain a cuboid, this can be written in dimensional form:

$$(1-p)\Delta(bHL_b) = -\langle q\rangle b\Delta t. \tag{53}$$

Here, the left hand side describes the change of sand volume. The parameter p is the porosity of sand. Sand grains come in all shapes and sizes and cannot pack together extremely well,

so there is a lot of empty space between them (*Chen and Miedema*, 2013). And in this empty space water still resides, hence it has to be accounted for. The width of the channel is denoted by b. There is no need to worry because the 1D problem suddenly has a width. By assuming the basin width to be constant over time, i.e. volume changes only due to L_b and H, it drops out on both sides. The right hand side features the change of water volume. The volume balance has to be rewritten a little bit, to give an expression for evolution of time. Assuming a fraction a of the sand transport goes to length, and a fraction $1-a$ to depth, the dimensional equations for time evolution can be written as

$$\Delta L_b = -\frac{a}{(1-p)}\frac{\langle q \rangle}{H}\Delta t, \tag{54}$$

$$\Delta H = -\frac{(1-a)}{(1-p)}\frac{\langle q \rangle}{L_b}\Delta t. \tag{55}$$

To formulate these expressions in their dimensionless form the scaling relations will once again be used. Net transport $\langle q \rangle$ will be scaled with γU^3, and the rest of the scaling relations can be found in equation (5), with the reminder that $U \sim \sqrt{g/H}Z$. The depth H is scaled by a constant H_0. These scaled relations yield:

$$\Delta \ell = -a\frac{\langle q \rangle}{H^3}\Delta \tau, \tag{56}$$

$$\Delta H = -(1-a)\frac{\langle q \rangle}{\ell H^3}\Delta \tau. \tag{57}$$

Here, τ is a morphological timescale, that is defined as

$$\tau = \frac{\gamma g Z^3}{H_0^3(1-p)}t. \tag{58}$$

The basin will stop transporting sand when an equilibrium has been reached. Figure 4 shows when equilibria can be considered stable following Escoffier's paper on the stability of tidal inlets (*Escoffier*, 1940). When transport leads to an equilibrium, the transport on the other side should go in the opposite direction. Negative transport indicates sand moving out of the basin, hence it makes the basin larger. His assumption was that tidal flow mainly tries to let the basin grow. Transport due to waves also plays a role in time evolution, as does sea level rise. Those respectively cause closure and lengthening/deepening of the tidal basin (*Beets et al.*, 2000).

2.6 Structure of written code

The toolkit necessary to solve our problem has now been created. The only thing left to do in order to find results is to create a script that runs the numbers. The structure of the main script is depicted in Figure 5. An important part is the loop seen in the middle of the flow chart, which describes the process for iteratively determining the linear friction coefficient λ.

Equation (14) is used to calculate λ. As can be seen, it depends on a prefactor which

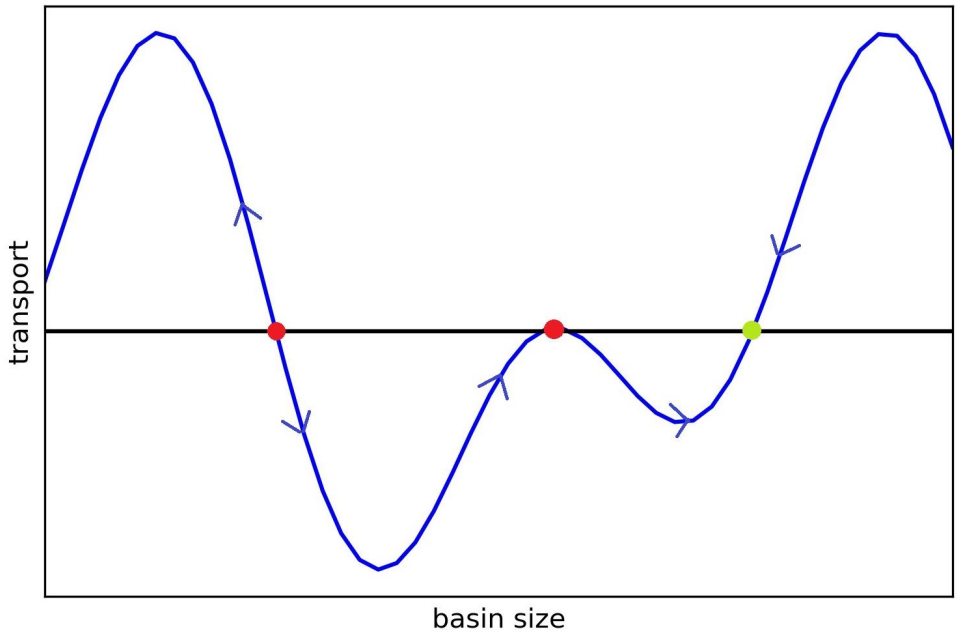

Figure 4: A fictional transport curve used to clarify the theory on stability of equilibria. Red dots mark unstable equilibria and the green dot shows a stable equilibrium.

has been called α here. However, this new parameter also depends on the water depth. So already the first major thing to note is: $\lambda = \lambda(H)$. This is one of the reasons why the dimensionless equations depend on water depth in the first place. Secondly it can be seen that in order to calculate the friction coefficient a velocity is required. In order to bypass this, an initial value of $u_{start} = 1$ is inserted to find a starting value for λ. Using this friction coefficient, $u_0(x)$ can be calculated. Now that a values for $u_0(x)$ have been found they can be plugged into equation (14) to find a new value for the friction coefficient. In this case $u \approx u_0$, because most of the energy is stored in the dominant term anyways. Then the two values for λ are compared to one another. If they deviate more than 10^{-3}, the process is repeated with the new value for λ, until it has converged enough.

After having calculated the friction coefficient, the script merely has to calculate all the scaled complex velocity components at the entrance of the basin, by using the equations derived in subsection 2.4. Thereafter they are used to calculate the transport corresponding to that point. This process is repeated for multiple lengths and depths, until the maximum length and depth have been reached. The script for time evolution is similar to this. The only difference being that it uses the equations for time evolution to determine the size of the basin, used for the next iteration.

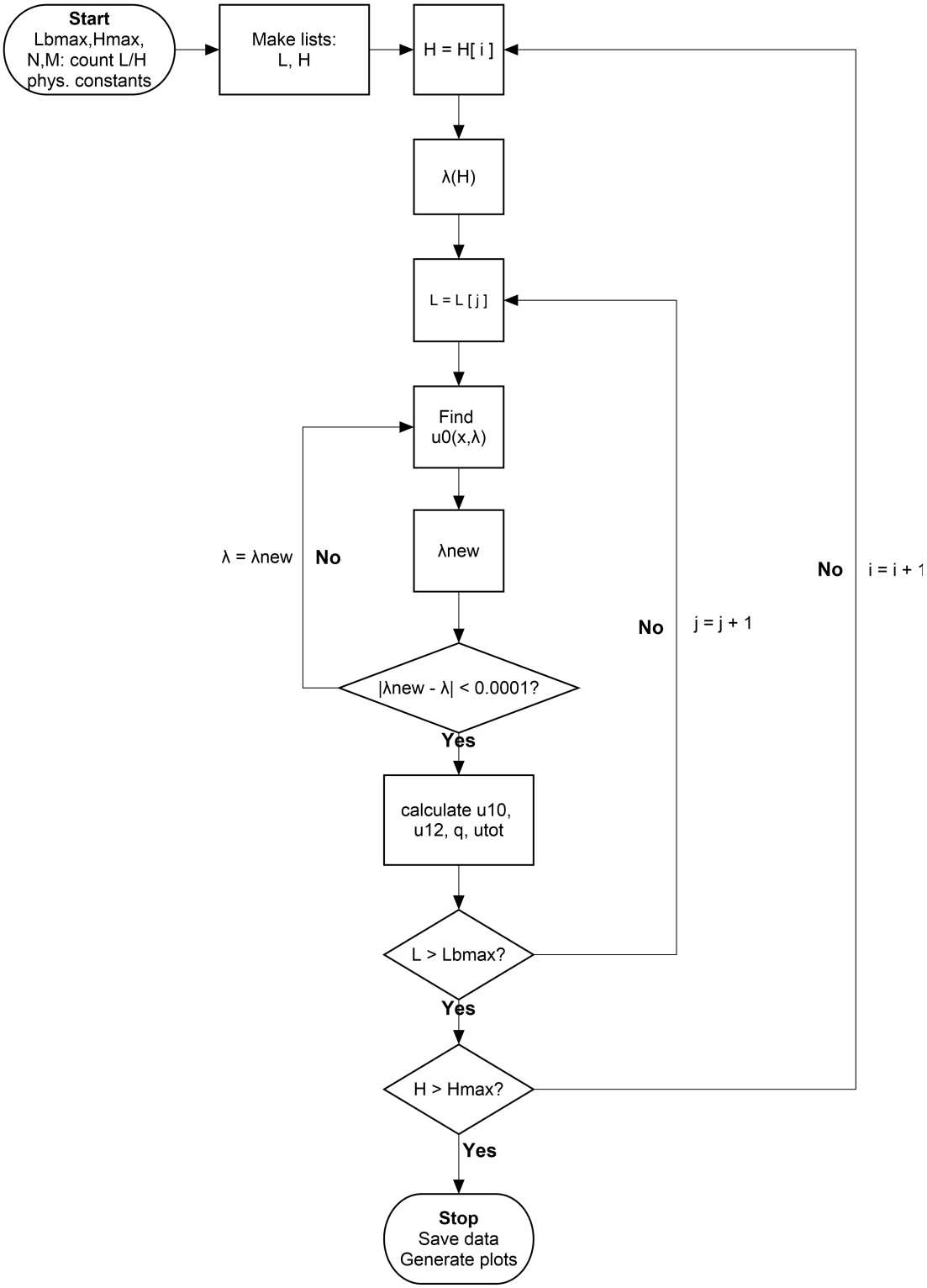

Figure 5: Flow chart for calculating velocities and sand transport for different lengths and depths of the tidal basin. The most time consuming part is the loop for iteratively determining the linearised friction coefficient λ. Lbmax and Hmax are the maximum (scaled) length and depth up to which velocity/transport has to be calculated. N and M define the resolution of the plots: N steps from 0 to Lbmax and M steps from 0.1 to Hmax. The symbols i and j are the iteration counters for respectively depth and length.

3 Methods

To find equilibria, the transport has to be calculated for different scaled lengths and depths of the basin. In order to do these calculations, some numerical values are required. Here, values are used that are representative for coasts along the North Sea. The period of a semidiurnal tide is set at 12 hours and 25 minutes; this corresponds to an angular frequency of $\omega = \frac{2\pi}{T_{sd}} = 1.405 \cdot 10^{-4}$ s^{-1}. The drag coefficient (c_d) is estimated to be $2.5 \cdot 10^{-3}$, based on observations. The scale for the height deviation (Z) is 1 m. The calculations are done on a 500x300 grid, with the scaled length ranging from 0 to 2π (1 tidal wavelength) and the scaled depth ranging from 0.1 to 5 (1 - 50 m). Hence H is scaled by $H_0 = 10$ m; for that depth $L_t \approx 70$ km is found. These results can be used to verify the existence of (stable) equilibria and to find the dominant hydrodynamic processes.

The porosity of sand (p) is estimated at 0.4 (*Bear*, 1988), and the parameter γ is $\sim 10^{-5}$ s^{2}m^{-1}, based on observations. All numbers combined lead to a morphological timescale of $\tau \approx 1380$ yr. The time evolution is cut into 12000 steps of $\Delta t = 0.5$ yr, which corresponds to a total of 6000 years. The script uses the dimensionless time step $\Delta\tau$, where a value of $\Delta\tau \approx 1/2760$ corresponds to half a year.

Experiments for sea level rate will be performed with three different values, from which the first two stem from the IPCC fifth assessment report (*Church et al.*, 2013) and the latter from the paper of Beets and van der Spek:

1. Current-day: 1.7 mm/yr,
2. RCP 8.5 scenario: 11.2 mm/yr,
3. Holland coast in 6000BP: 3 mm/yr.

The first two values are used to describe future evolution scenario's, whereas the third looks back in the past of the Dutch coast and tries to see if the model finds the same behaviour as what happened in reality (closure of basins). To complete the analysis, a constant transport due to waves will be added to the model. Given that at small sizes the basins are expected to close, a value can be found for this transport that can be compared to real observations.

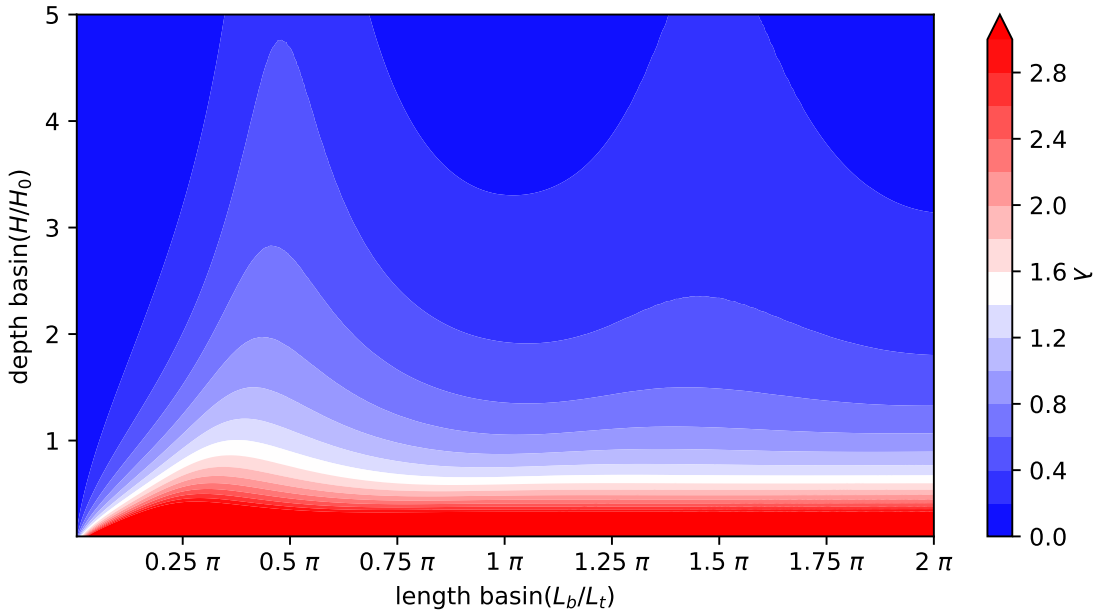

Figure 6: A contour plot of the linear friction coefficient for scaled basin length and height. The horizontal axis depicts the length of the basin, scaled by the frictionless tidal wavelength divided by 2π. The vertical axis depicts the depth scaled by a reference value $H_0 = 10$ m. Red colours correspond to higher values of λ.

4 Results

The goal of this section is to let the mathematical framework laid down in the former sections come to fruition. It will show the main results, which help solidify the theory behind tidal asymmetries and sand transport.

An integral part of the calculations was in fact the linearised friction coefficient, that made an appearance in all velocity components. Figure 6 shows the values for λ for different scaled basin lengths and depths. The smaller the depth, the larger the value for the friction coefficient becomes. This is not surprising in the least since the prefactor α, given in equation (10), increases with decreasing H, as $\alpha \propto H^{-3/2}$.

Figures 7 and 8 show the solutions for the zeroth-order problem, the dominant terms. Figure 7 shows the dimensionless velocity amplitude at the entrance of the basin for varying length and depth. The velocity goes to zero for very low basin lengths and depths. This is as expected, since at very low depths and lengths, there is barely a tidal basin to begin with.

This picture shows clear peaks at (slightly less than) the scaled length of $\frac{\pi}{2}$, a quarter of the frictionless tidal wavelength. At roughly the scaled length of π, half a tidal wavelength, the velocity almost drops to zero. The same is repeated for $\frac{3\pi}{4}$ and 2π. This means that $|\hat{u}_{01}|$ shows the behaviour of a standing wave, with nodes at nearly half and one tidal wave-

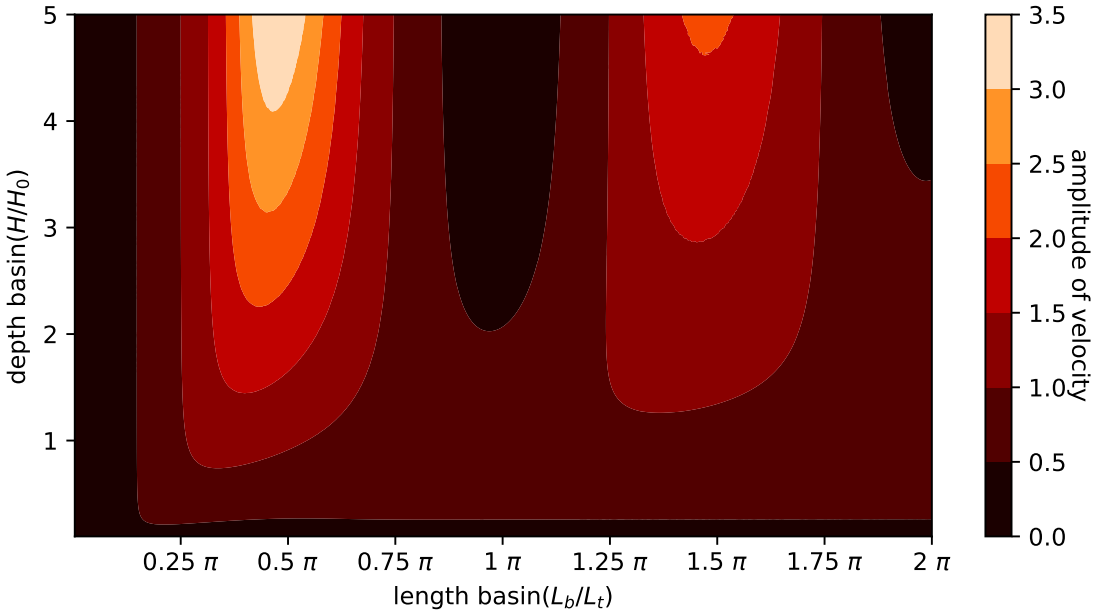

Figure 7: Colour plot of the dimensionless amplitude of the dominant velocity term at the entrance of the basin. Darker colours resemble lower velocities.

length and anti-nodes at almost (three-)quarter tidal wavelength. The resonance peaks have slightly shifted to lower lengths because of the effects of friction. When compared to Figure 6 it becomes apparent that larger friction corresponds to a larger shift.

Other interesting behaviour occurs when studying Figure 8, that show along-channel profiles of the amplitude of free surface variations and velocities and their respective phases for certain depths. The scaled length of the basin is chosen at $\ell = \pi$, which is not the most realistic length, given that it corresponds to dimensional lengths ranging from 225 to 383 km in this figure. This value is chosen regardless, since some behaviour is better noticeable than for lengths only up to 100 km. For depths of 20 and 30 m the behaviour of a standing wave at the entrance are again observed in Figure 8c. At H=10 m the resonance features are slowly fading away, because of dampening due to friction. This means that the velocity amplitude at the entrance mostly depends on the incoming wave, as the reflected, outcoming wave at the entrance has weakened too much due to bottom friction.

Figure 8b and 8d show along-channel phase profiles. The phase of the surface elevation tells when high tide will occur. Figure 8b shows that at the end of these basins the phase is roughly π. This means that if there is a maximum elevation at the entrance, there will be a minimum at the end of the basin, and vice versa. Similarly, the phase of the dominant velocity tells when maximum flood occurs. When comparing 8b and 8d it becomes clear that the phase difference between velocity and surface elevation becomes smaller when moving further into the basin. This means that flood follows high tide more quickly towards the end of these basins. Figure 9 shows what that would look like in a 10 m deep, 45 km long basin.

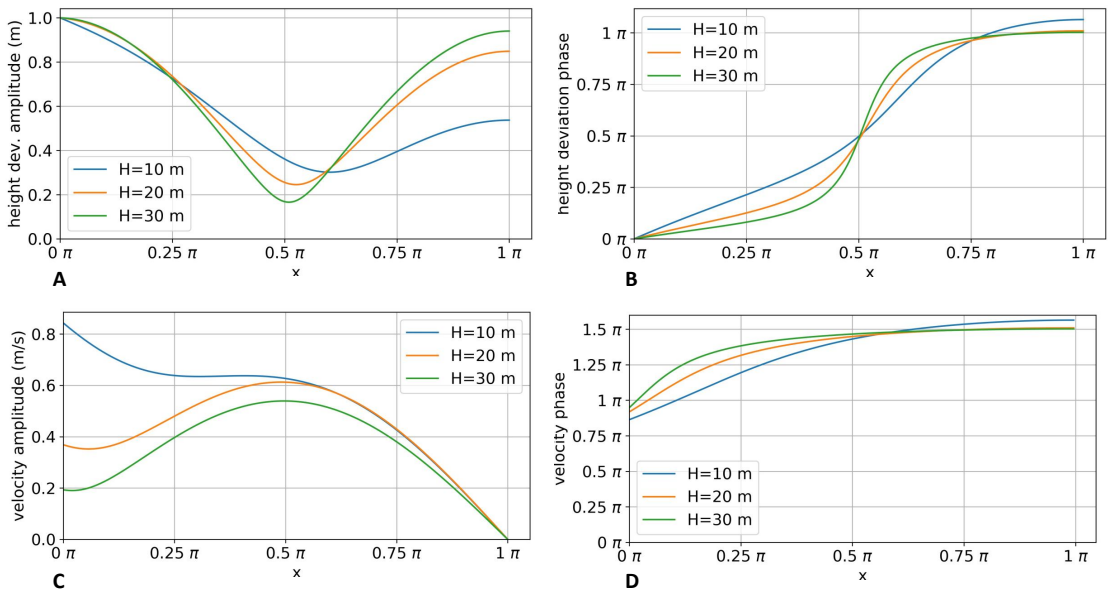

Figure 8: This figure features four profiles over the length of a tidal basin of scaled length $\ell = \pi$ concerning different aspects of the dominant tide. Each picture shows three different scenario's with varying basin heights. The figures show the following: **A** dimensional amplitude of height deviation; **B** phase of height deviation; **C** dimensional amplitude of velocity; **D** phase of velocity.

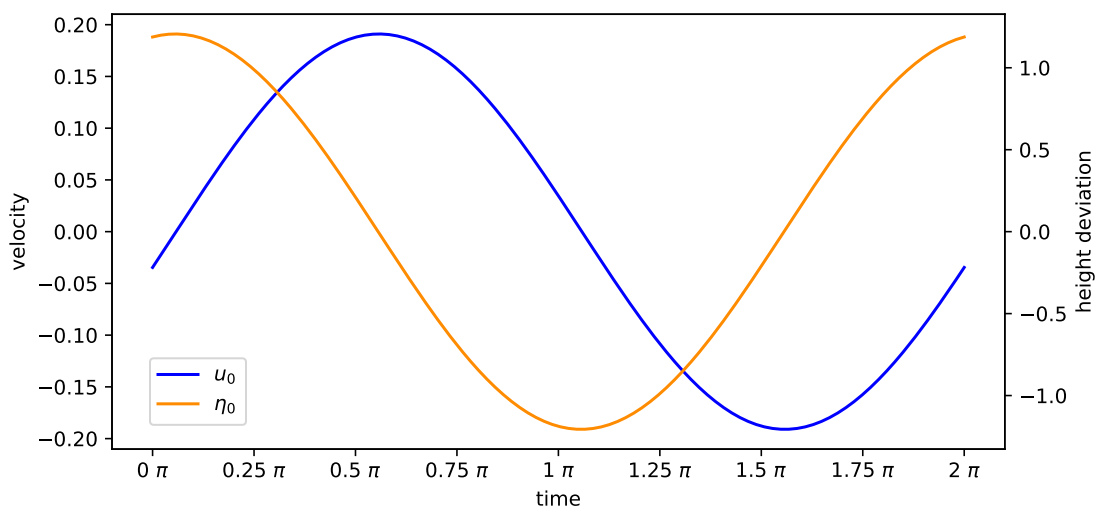

Figure 9: This figure shows the dominant dimensionless tidal velocity (blue line) and the dominant dimensionless tidal height deviation (orange line) at x = $\frac{\pi}{10}$. The depth of the basin is 10 m, with a total length that corresponds $\ell = \frac{\pi}{5}$ (45 km). A phase difference of $\frac{\pi}{2}$ is observed between the two lines. The values on the right axis are for the height deviation and the values on the left side are for the velocity.

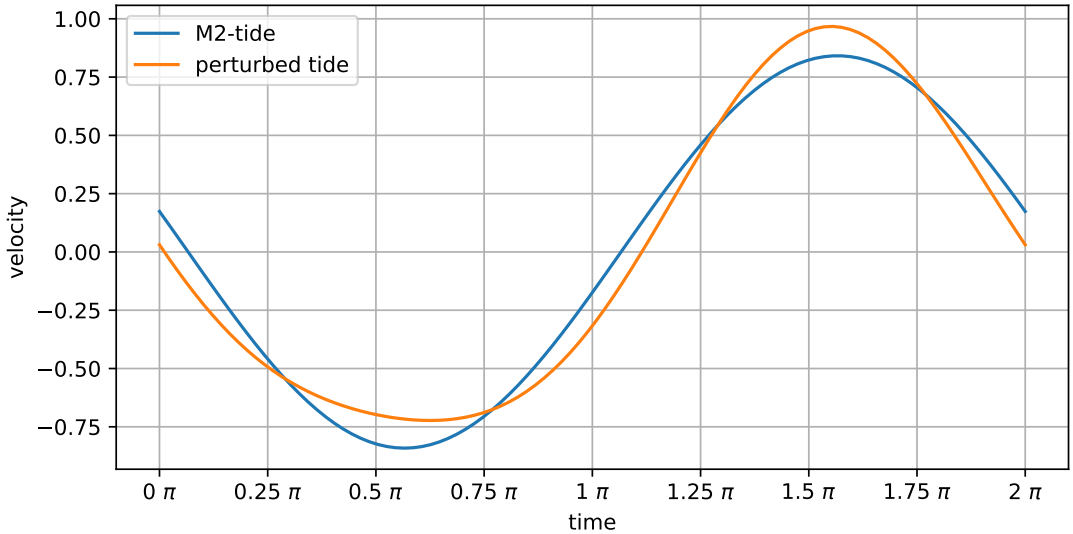

Figure 10: Scaled velocity during one tidal period at the entrance of the tidal basin (x=0), with a depth of 10m and scaled length of $\frac{\pi}{4}$ ($\approx$ 56 km). All velocity terms are taken into account. The blue line shows the dominant flow, and the orange line shows dominant flow, plus the $O(\epsilon)$ perturbations. The perturbations tend to be mostly positive, hence this depicts an flood-dominated basin.

In this model, sand transport over a longer period of time is dependent on tidal asymmetries. Hence it would only be logical to show that the model actually produces such asymmetries. Figure 10 shows such a velocity profile over one tidal period at the entrance of the basin. The basin has a depth of 10 m and a length of 56km. Judging from the distance between the orange and the blue line (resp. the line with and without asymmetries), the perturbations are of the order cm/s. The perturbations are mostly making the flow more negative, so the specific tidal basin depicted is flood-dominated. This means that in order for the theory on sand transport to hold, the transport has to be positive.

One of the points of interest is to find the dominant hydrodynamic process for sand transport. Before actually showing the transport it is interesting to look at the velocity amplitudes of each independent term, since the magnitude of the transport heavily relies on this. Figure 11 shows the dimensionless velocities, without the Froude number taken into account. For larger depths, the competition is clearly held between the divergence of excess mass flux and advection. Without looking at the phase difference and actual transport, it has already become apparent that the depth-dependent friction will play a minor role in most cases, in comparison to the formerly mentioned terms. The sign (and magnitude) of sand transport also depends on (the cosine of) phase difference between M2- and M4-tide, the values of which are observed in Figure 12. In subfigure d a constant value of -1 appears for the residual term. This is in line with equation (41), which shows a function plus its complex conjugate. Because of this, the complex amplitude of the residual term is no longer complex. Thus its argument will be $\pm\pi$ by default, leading to $\cos(\pm\pi) = -1$. Because of this all transport due to residual flow is negative, as it opposes positive transport due to waves.

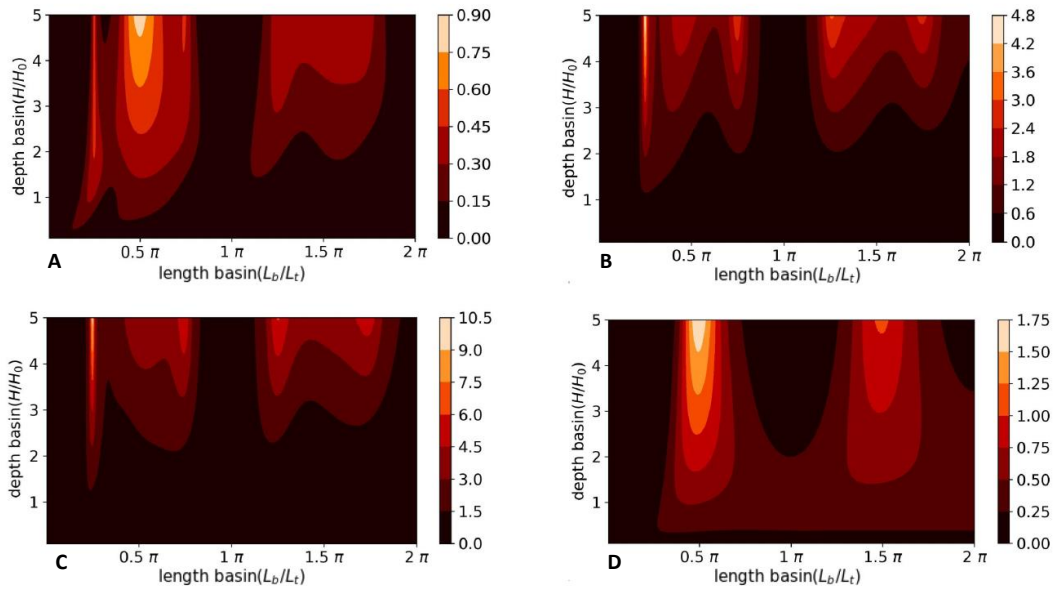

Figure 11: Colour maps of scaled M4-velocities(**A**-**C**) and M0-velocities(**D**) at the entrance of the tidal basin, without prefactor ϵ. The following overtide terms are shown: **A** depth-dependent friction;**B** advection; **C** divergence of excess mass flux. **D** shows the only residual term, from the divergence of the excess mass flux. These values would be of the order of centimetres, going to millimetres for smaller depths.

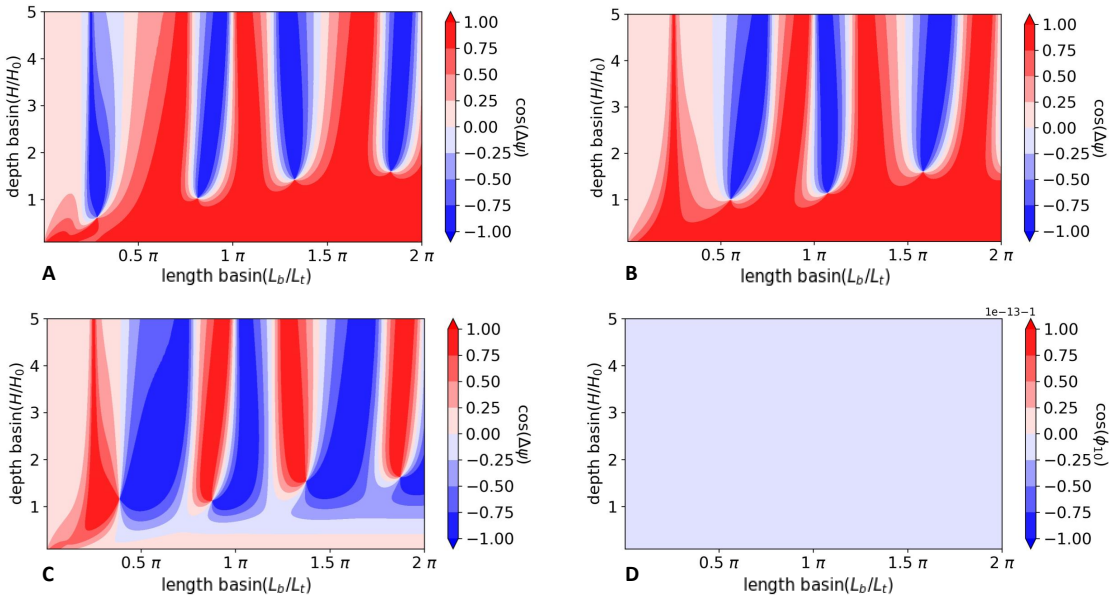

Figure 12: Colour maps showing the cosine of the phase difference ($\Delta\psi$) between the M2- and M4-velocities at the entrance of the tidal basin (x=0). The following overtide terms are shown: **A** depth-dependent friction;**B** advection; **C** divergence of excess mass flux. **D** features the cosine of ϕ_{10}. Red colours indicate a positive sign, blue colours indicate a negative sign.

The cornerstone of the research is given by Figures 13 and 14: (scaled) values for net transport. The black lines in all (sub)figures mark equilibria, points where transport becomes zero. To put it shortly, those equilibria exist in this idealised model. Moreover, these figures also provides insight on the stability of those equilibria, by following a similar approach as Escoffier. If transport is negative, the basin increases in size, hence you move towards the top-right of the figure, i.e. both H and L_b become larger. If transport is positive, the basin size decreases. An equilibrium can thus be considered stable if there is a positive transport to the (top-)right and a negative transport towards the (bottom-)left in the figure.

As a small check to see if there are no discrepancies in the theory, let's look whether the ebb-dominated basin, described in Figure 10, really has positive sand transport. The scaled depth in this case is 1, and the scaled length is $\frac{\pi}{4}$. Figure 13, which shows the total transport with all contributing terms, then demonstrates that the sand transport is indeed positive. Escoffier argued that tidal asymmetries cause a sediment discharge directed outwards of the basin. For scaled lengths until roughly $\frac{\pi}{4}$ this does not seem to be the case in this model. The inlets within a reasonable domain for the North Sea appear to have no stable equilibrium (besides being closed), based solely on the modelled tidal current. The smallest stable inlet, only maintained by tidal currents, has the dimensions of roughly $\ell = \frac{8\pi}{10}$, with $H = 20$ m. This translates to a basin longer than 250 km, which is very long.

Depth-dependent friction (Figure 14a) is now shown to really be a secondary effect, as it is severely outperformed by the other contributors. When comparing Figures 14b and 14c it is shown that advection and divergence of excess mass flux both have similar effects. At smaller depths all overtide terms try to close the basin, whereas the residual, as expected, forces it to grow. Most competition is observed between the residual flow and the overtide flow of EMF. Most of the behaviour seen in the total transport in Figure 13 can be explained by adding Figures 14c and 14d. The residual flow was explained as a current that compensates for the mass flow towards the basin caused by tidal waves. For all basin sizes the transport caused by the residual term is indeed demonstrated to be negative.

Figure 15 shows the evolution of a tidal inlet starting from eight different initial conditions for length and depth over the course of an immense 200,000 years. Realistically, time scales of interest are around 6000 years (see e.g. *Beets et al.*, 2000). The purpose of this picture is showing how the system tends toward stable morphodynamic equilibria, or how they close after a certain time. The transport in this figure is solely decided by the tidal flow, as depicted in Figure 13. The stable and unstable equilibria become more apparent here. Following the earlier mentioned stability criterion the left sides of the positive transport bulges are stable, whereas the right sides are unstable. The time series of net sand transport for case 8 is shown in Figure 16. It reveals that the system reaches an equilibrium after 125,000 years. Cases 1 to 4 show more realistic basins, with lengths up to 120 km, whereas cases 5 up to 8 show basins that are larger than 200 km.

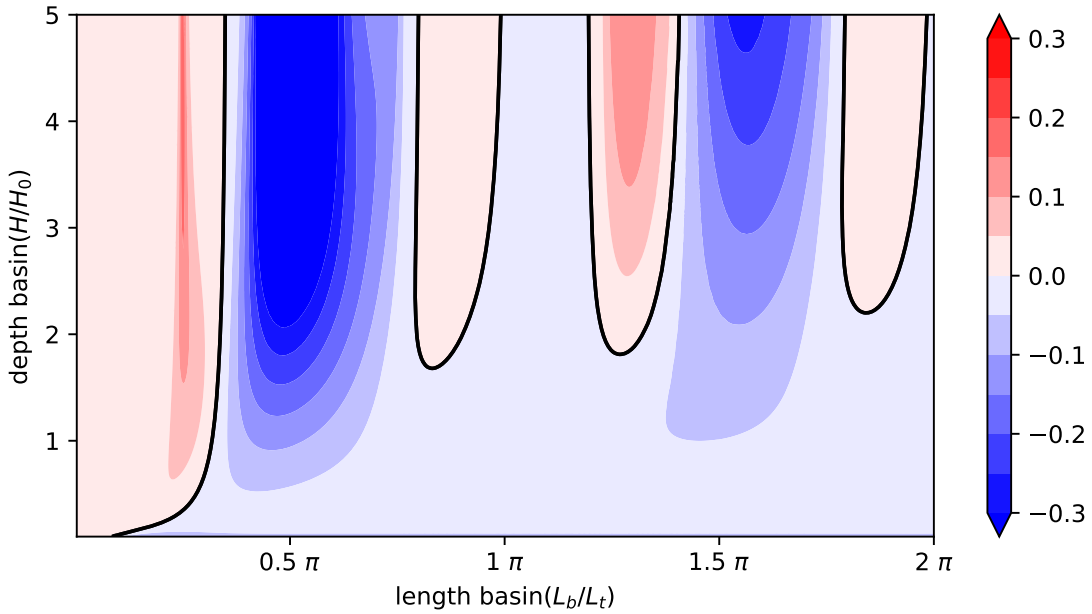

Figure 13: Calculated scaled transport due to tidal currents with all three hydrodynamic processes taken into account. Red tints show positive transport, whereas blue tints show negative transport. Black lines mark equilibria.

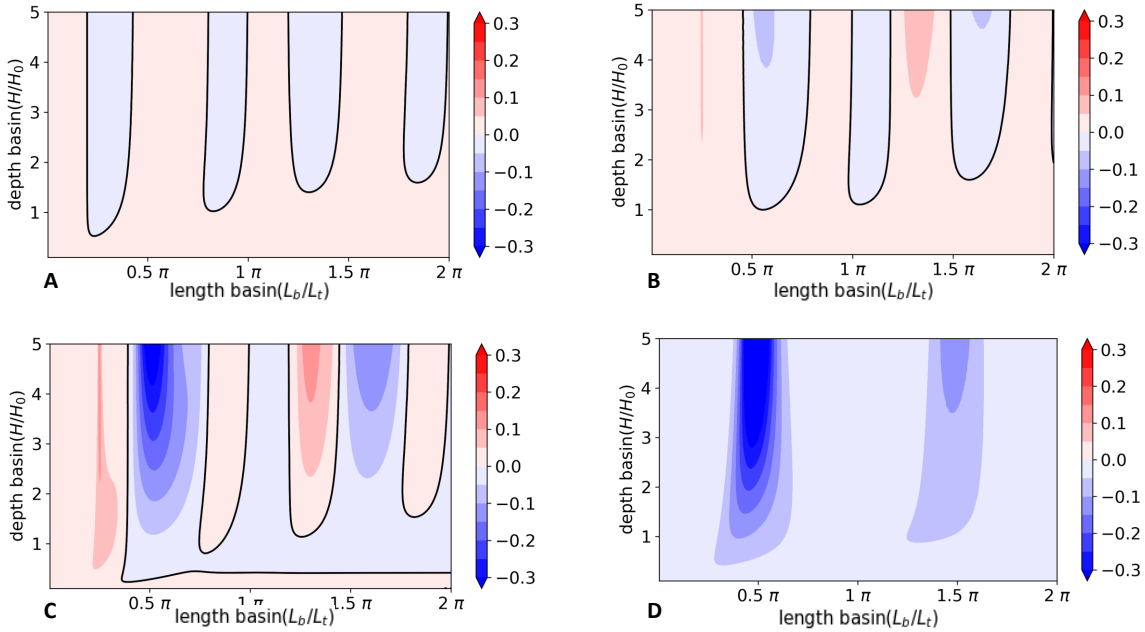

Figure 14: Calculated scaled transport with different hydrodynamic processes taken into account. Red tints show positive transport, whereas blue tints show negative transport. Black lines mark equilibria. The contourplots feature **A** depth-dependent friction; **B** advection; **C** divergence of excess mass flux, overtide; **D** divergence of excess mass flux, residual.

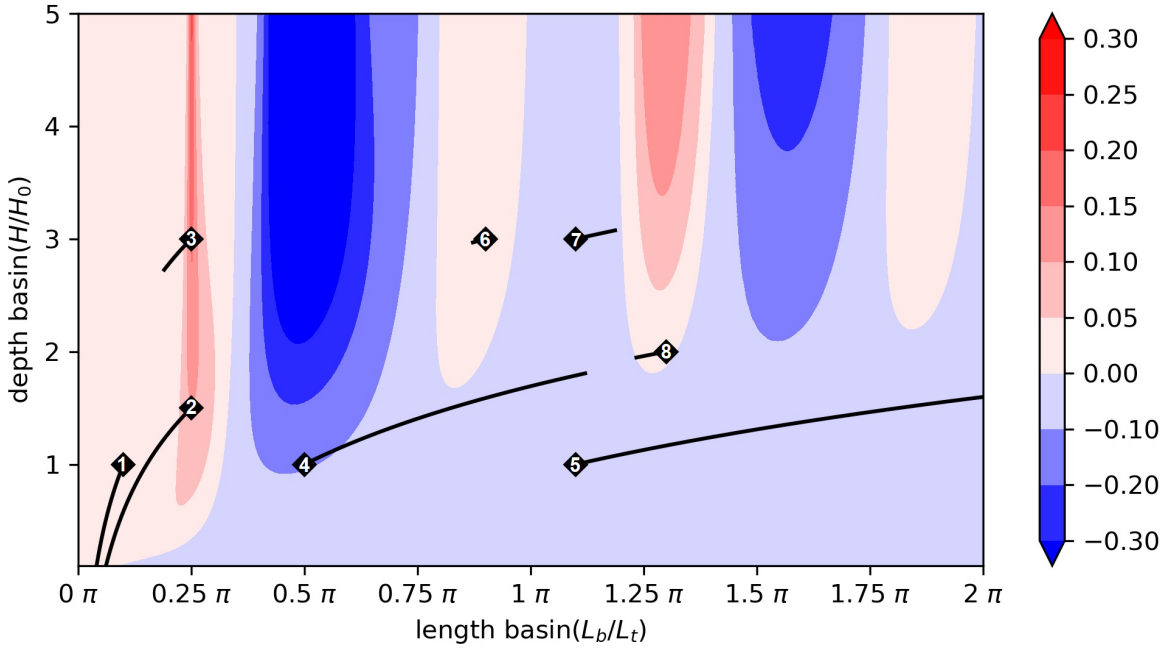

Figure 15: Curves showing the scaled evolution of 8 tidal basins of different sizes, during a time period of 200,000 years. The fraction coefficient is 0.5, meaning that half of the sand changes the length and half of it the depth. No sea level rise or transport due to waves is accounted for. Diamonds mark the initial sizes of the basins. Pink regions have positive sand transport (shrinking inlet), blue regions have negative sand transport (growing inlet).

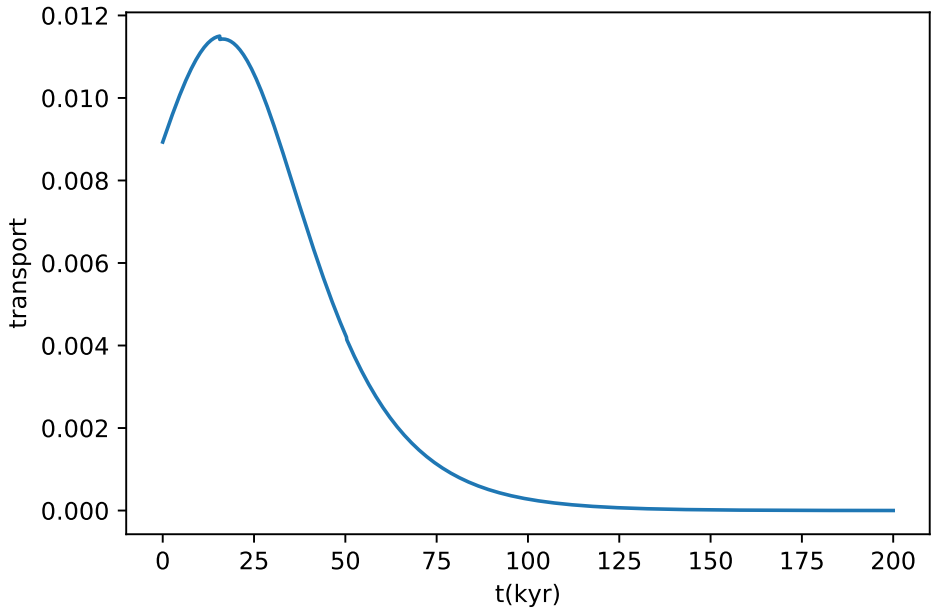

Figure 16: Time series of transport over 200,000 years corresponding to case 8 in Figure 15 ($\ell = 0.2\pi,\ H = 15$ m). The transport is positive, meaning the basin expands. After 125,000 years the basin is almost in a stable equilibrium.

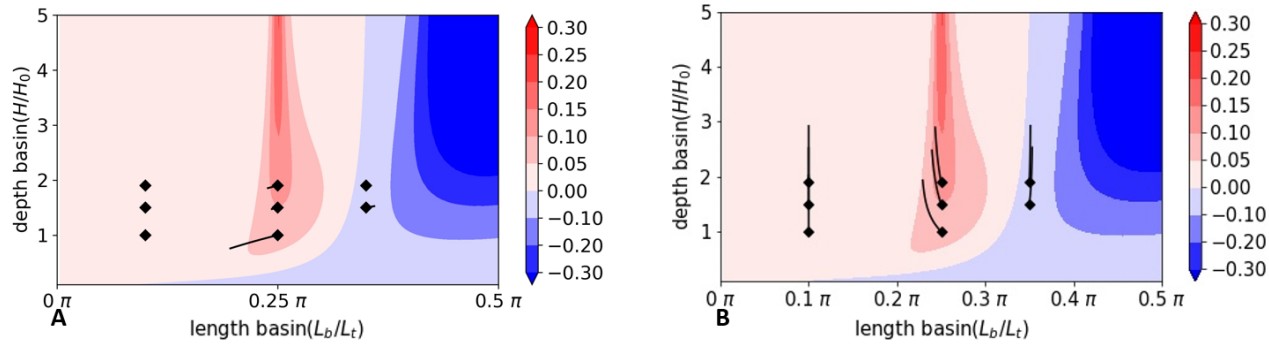

Figure 17: Curves showing the scaled evolution of 8 realistically sized tidal basins of different sizes, without transport due to waves, during a time period of 6000 years. The fraction coefficient is 0.5. Scenario **A** has no sea level rise and **B** has a current-day SLR of 1.7mm/yr.

Figure 17 shows the time series of several cases, representative for the Holland coast, over a time of 6000 years. Figure 15a demonstrates that transport solely due to tidal currents is insufficient to close a reasonably sized tidal basin. In the case of $\ell = \frac{\pi}{4}, H = 10$ m, a scaled transport of ∼0.1 is observed. Multiplying that by γU^3 and converting seconds to years gives a dimensional transport $q_{dim} \approx 32$ m^2/yr. Assuming half of that goes into length evolution ($a = \frac{1}{2}$), this leads to a dimensional rate of change $\frac{\Delta L_b}{\Delta t} \approx -2$ m/yr. Assuming this to be constant over 6000 years this would mean a change in length of roughly 12 km. The actual length change was around 11 km ($\Delta\ell \approx \frac{\pi}{20}$) after 6000 years.

Figure 17b adds a current-day sea level rise of 1.7mm/yr to the system. The system is clearly dominated by the sea level rise. In all cases the transport due to tidal currents is too weak to compete with sea level rise. This can be quantified by looking at the same case as before. Half of the dimensional transport spread over a length of 56 km leads to the dimensional rate of change $\frac{\Delta H}{\Delta t} \approx -0.2$ mm/yr. This is definitely not enough to compensate for 1.7mm/yr SLR. When sand transport due to waves becomes even less, the basin simply drowns. Figure 17b points out a major flaw in the model: with increasing depth the frictionless tidal wavelength increases. Having a constant scaled basin length with rising sea level would mean that the basin is constantly growing in dimensional length as well, even if it is presumed to remain constant.

Figure 18 shows time series of multiple basins, depending on tidal currents, waves and sea level rise. The scaled transport due to waves q_{wave} is a constant, estimated at 0.1, such that some basins are actually capable of closing, as has happened along the Dutch coast. Figure 18a shows that for lower depths without any sea level rise in some cases basins close. However in Figure 18b, when accounting for a modern day sea level rise (1.7 mm/yr), all cases depict basins that can barely compete with SLR. When going back 6000 years in the past (assuming a sea level rise of 3mm/yr) the cases in Figure 18c put up even less of a struggle. Using the worst case scenario of the IPCC, RCP 8.5 (11.2 mm/yr), all of the basins in figure 18c will become deeper so fast the deposition has almost no time to respond at all.

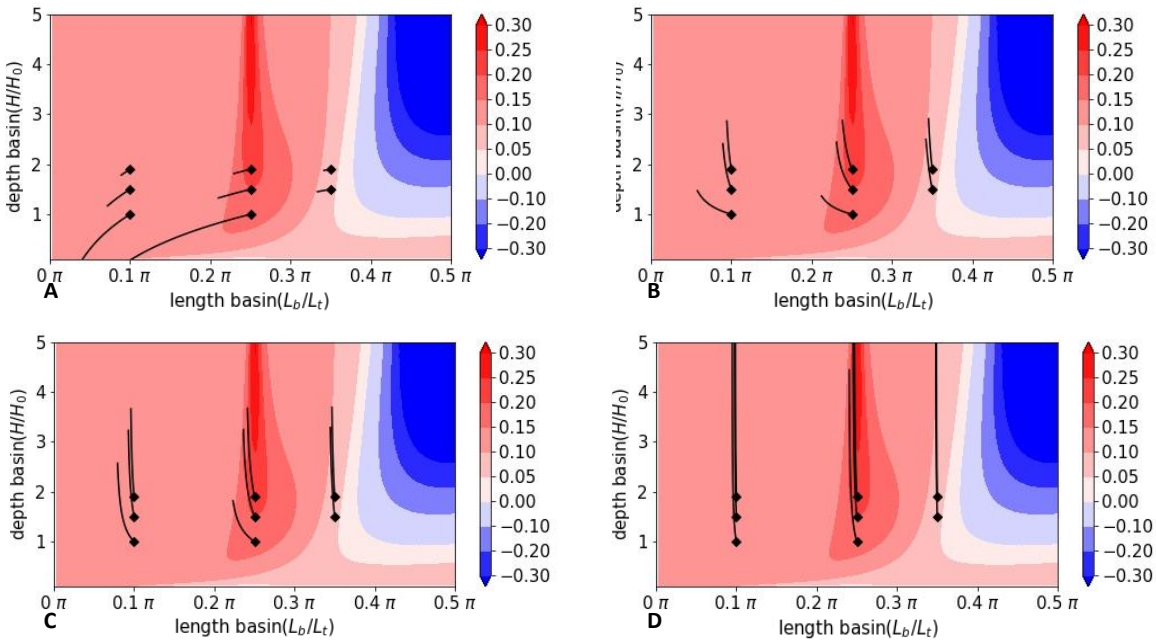

Figure 18: Curves of the scaled evolution over 6000 years with due to tidal flow, waves and sea level rise for four different sea level rise scenario's. In all figures a constant transport due to waves $q_{wave} = 0.1$ is added. The different SLR scenario's are: **A** 0 mm/yr, **B** 1.7 mm/yr, **C** 3 mm/yr and **D** 11.2 mm/yr.

Contour plots of critical sea level rise are shown in Figures 19 and 20. The results show that the critical sea level rise is way lower than for example the current-day SLR of 1.7mm/yr, let alone the RCP8.5 scenario. These results explain the behaviour seen in Figures 17 and 18. Of course these critical values can be increased by adding larger transport due to waves. This can be seen when comparing the case without waves (Figure 19) and the case with waves (Figure 20). For lower depths, the critical value rises most. This has to do with the scaling of q, which is $\propto u^3$. From equation (5) it follows that the scaling of u is $Z\sqrt{g/H}$, meaning that when making the scaled transport dimensional it has to be multiplied with a prefactor $Z^3(g/H)^{3/2}$. Hence, as an example, the same value for scaled transport at depth H = 10 m corresponds to a higher dimensional transport than H = 40 m. Then the conversion from scaled length ℓ to dimensional length L_b also increases with increasing depth, meaning that for larger depths less sediment has to be spread out over a larger length.

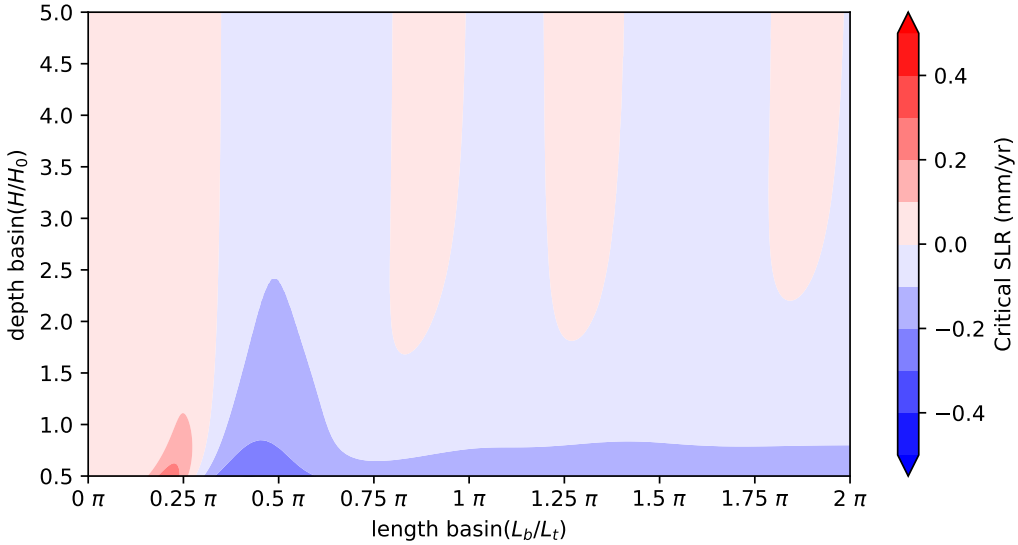

Figure 19: Contour plot of critical sea level rise in mm/yr, when accounting for only sand transport due to tidal asymmetries. The fraction of sand transport into depth is $a = 0.5$. These numbers are way lower than current-day SLR.

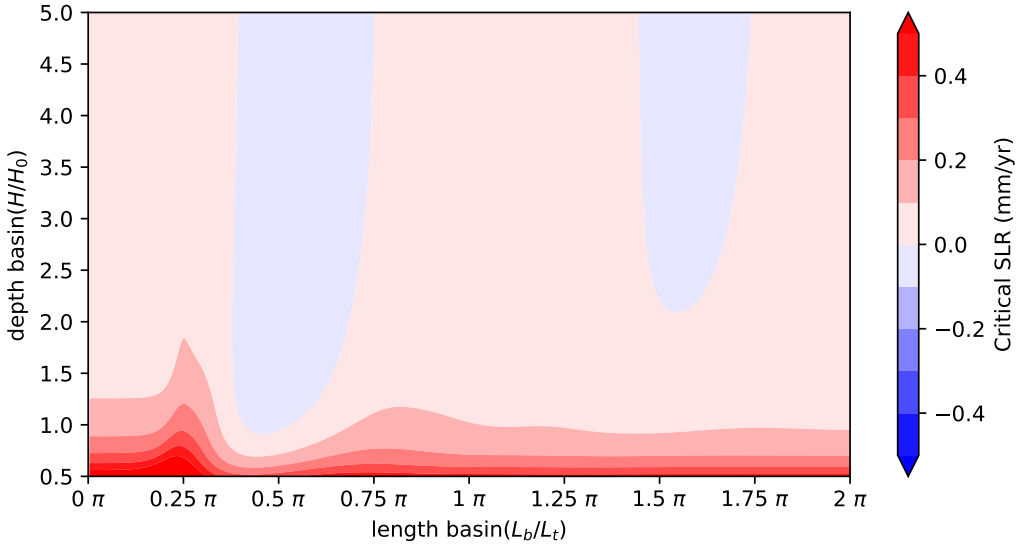

Figure 20: Contour plot of critical sea level rise in mm/yr, when accounting for both sand transport due to tidal asymmetries and a a constant scaled transport due to waves $q_{wave} = 0.1$. The fraction of sand transport into depth is $a = 0.5$.

5 Discussion

This study shows that evolution and stability of tidal basins are determined by sand transport due to tidal currents, deposition due to waves and the creation of accommodation space by sea level rise. Tidal currents can lead to both net import as export, depending on the length and depth of the basin. In the domain of interest, short and shallow basins, tidal flow always leads to net import. Inlets can thus only be stable with sufficient sea level rise. Beets and van der Spek (2000) discussed how most basins along the Holland coast closed during the Holocene because of decreasing sea level rise. Some inlets managed to stay open due to tidal currents having been strong enough. Because of this, inlets like the Schelde and the Wadden Sea have stayed open until now.

Unfortunately, the Wadden Sea is at risk of drowning, should a critical sea level rate be exceeded (*Wang et al.*, 2012). With current sea level rise this should not happen, but according to IPCC reports (*Church et al.*, 2013) sea level rise is still increasing. The idealised model is able to find such critical SLR values, but they are already way lower than the current 1.7 mm/yr. Implications of a faster sea level rise would be that tidal flats will not be exposed during ebb, causing a major upheaval in the ecological system. The mudflats are nutrient-rich and thus provide a good breeding spot for small sea animals such as mussels and oysters (*Reise*, 2005). Migrating birds often use these flats as resting spots, which becomes impossible once the tidal flats have drowned. The Frisian Islands are also a very popular tourist destination, with over one million Dutch tourists each year (*CBS*, 2016). Loss of much of the Wadden Sea would heavily impact the local economy, as those tourists together spend nearly 300 million euros on a yearly basis. This indicates the relevance of studying tidal inlet systems; they were important for Bruges in the thirteenth century, they are important for the Wadden Sea in the present and they will be important in the future.

The calculations done are similar to those in morphological studies that are discussed in the review by de Swart and Zimmerman (2009), but a noticeable difference concerns the approach on how sand transport determines erosion and deposition inside the basin. Unlike in this research the bottom geometry is not flat and horizontal, because there is a real bottom evolution equation in play. This means the flow cannot be constantly described as if looking at a rectangular box. Critical velocities necessary to initiate sand transport are often taken into account, which have been ignored in this research, since it is assumed that most of the time the velocity will be higher than this critical velocity. However, implementations of such kinds in the model limit the time that can be evaluated. The model created in this research can easily run an evolution of 6000 years within fifteen seconds.

The concepts introduced by Escoffier (1940) are applied in many other studies (e.g. *Reef et al.* (2020) and references herein). In his approach, tidal flow would always amount to negative transport in a single inlet system and if this flow would reach a certain critical velocity, it would be enough to compensate for the transport due to tidal waves. This was used to introduce the concept of stability, which is also used in this research. Although most of it is still in line with this research, the results showed that within the domain of interest the tidal flow leads to sand import.

This model considers only sand with a porosity of 0.4. Realistically, sand grains come in all sizes and the model would react differently to fine or coarse sand. Sediment would more realistically be a mixture of sand and mud (*Bear*, 1988). In the present model, the only variables that can take this into account are the porosity p and the parameter γ. The last point concerning the transport is the assumption that $q \propto u^3$. This only takes bottom transport into account. Possible other ventures are taking floating dust into account, with a sediment discharge $q \propto u^5$, the formulation of Engelund-Hansen (*Engelund and Hansen*, 1967).

One issue of this research is the domain for which the solutions can be considered valid. The perturbation analysis only holds for a small value of the Froude number $\epsilon(H)$. Choosing when $\epsilon \ll 1$ is a very subjective business; one could choose 0.05, 0.1 or 0.3 and every person could make a valid case. In this research the scaling of the height deviation Z is fixed at 1 m, meaning that for some low value of H the criterion of a small Froude number is violated. Introducing a varying Z, which becomes smaller at lower depths would increase the validity of transport values in that domain.

Forcings on the tide can also be altered. The current forcing of the tide is an M2-tide with constant peaks, disregarding local bathymetry. Possible ventures could include but are not limited to an adding a M4-tide or S2-tide (jump or neap tide) to the forcing. Or by setting the fundamental frequency to be that of a diurnal tide (one ebb and one flood per day). Research indicates that in the Wadden Sea seasonal variations in M4-tides are extremely important for sediment transport (*Gräwe et al.*, 2014). This reinforces the idea of adding additional forcings at the open boundary of the system.

In short, the beauty of this model lies within its simplicity and the ability to work over longer periods of time. This distinguishing feature can be conserved while still making some adjustments: the basin has a slope; different sediments are modelled; instead of just using a M2-forcing, extra forcings are imposed on the open boundary; the height deviation Z varies; and so on. This opens the path to more realistic yet relatively simple modelling of tidal inlets.

6 Conclusions

Nonlinear terms in the shallow water equations create asymmetries in the tide, which induce net sand transport. The three nonlinear terms are depth-dependent friction, advection, and divergence of excess mass flux. The first two only generate M4-tide, whereas the latter also generates M0-tide. The primary aim was to find out if tidal basins are capable of reaching a stable morphodynamic equilibrium. It is shown that these equilibria can exist, depending on the balance between sand import/export due to tidal flow, sand deposition due to waves and creation of accommodation space by sea level rise.

Another goal was to find the dominant hydrodynamic processes that cause sand transport. This research indicates that divergence of excess mass flux is the dominant term in most domains, whereas depth-dependent friction always plays a secondary role. For short and shallow basins, representing the situation along the Dutch coast, the overtide terms cause net sand deposition, whereas the residual term causes net erosion. When adding all separate terms, the tidal flow causes net sand import in this domain.

The last objective was to test the response of the model to multiple scenario's of sea level rise and sand transport due to waves. It is found that, when the sea level rise is low, the basin indeed closes more easily due to tidal currents and waves. Tidal flow in the current model has no means of keeping the basin open, as it is always positive within the 'Dutch coast'-domain. This means that for slow enough sea level rise basins try to close. The critical rate when sea level rise dominates the system is found to be very low in the idealised model in comparison to realistic values for sea level rise.

References

Bear, J., *Dynamics of Fluids in Porous Media*, Dover Publications Inc., 1988.

Beets, D. J., van der Spek, and A. J. F., The Holocene evolution of the barrier and the back-barrier basins of Belgium and the Netherlands as a function of late Weichselian morphology, relative sea-level rise and sediment supply, *Netherlands Journal of Geosciences - Geologie en Mijnbouw*, *79*(1), 3–16, 2000.

CBS, 1,3 miljoen toeristen op vakantie naar de Wadden, 2016.

Chen, X., and S. Miedema, Porosity calculation in discrete element modeling of sand cutting process, 2013.

Church, J. A., P. U. Clark, A. Cazenave, J. M. Gregory, S. Jevrejeva, A. Levermann, M. A. Merrifield, G. A. Milne, R. S. Nerem, P. D. Nunn, A. J. Payne, P. W. T, D. Stammer, and A. S. Unnikrishnan, *Climate Change 2013: The Physical Science Basis. Contribution of Working Group I to the Fifth Assessment Report of the Intergovernmental Panel on Climate Change*, Cambridge University Press, 2013.

Colling, A., D. Park, and J. Wright, *Waves, Tides, and Shallow-water Processes*, Butterworth-Heinemann, in association with the Open University, 1999.

Davis Jr, R. A., and D. M. FitzGerald, *Beaches and Coasts*, John Wiley & Sons, 2009.

De Swart, H. E., and J. T. F. Zimmerman, Morphodynamics of Tidal Inlet Systems, *Annual Review of Fluid Mechanics*, *41*, 203–229, 2009.

Engelund, F., and E. Hansen, A monograph on sediment transport in alluvial streams, *Technical University of Denmark 0stervoldgade 10, Copenhagen K.*, 1967.

Escoffier, F. F., The Stability of Tidal Inlets, *Shore and Beach*, *8*, 114–115, 1940.

Gräwe, U., H. Burchard, M. Müller, and H. M. Schuttelaars, Seasonal variability in M2 and M4 tidal constituents and its implications for the coastal residual sediment transport, *Geophysical Research Letters*, *41*(15), 5563–5570, 2014.

Lodder, Q. J., Z. B. Wang, E. P. L. Elias, A. J. F. van der Spek, H. de Looff, and I. H. Townend, Future Response of the Wadden Sea Tidal Basins to Relative Sea-Level rise—an Aggregated Modelling Approach, *Water*, *11*(10), 2198, 2019.

Lorentz, H. A., Verslag Staatscommissie Zuiderzee, *Algemene Landsdrukkerij, The Hague, the Netherlands*, 1926.

Murray, J. M., *Bruges, Cradle of Capitalism, 1280-1390*, Cambridge University Press, 2005.

Ranasinghe, R., and C. Pattiaratchi, Tidal inlet velocity asymmetry in diurnal regimes, *Continental Shelf Research*, *20*(17), 2347–2366, 2000.

Reef, K., P. Roos, H. Schuttelaars, and S. Hulscher, Influence of Back-Barrier Basin Geometry on Multiple Tidal Inlet Systems: The Roles of Resonance and Bottom Friction, *Journal of Geophysical Research: Earth Surface*, *125*(3), e2019JF005,261, 2020.

Reise, K., Coast of change: habitat loss and transformations in the wadden sea, *Helgoland Marine Research*, *59*(1), 9–21, 2005.

Wang, Z. B., P. Hoekstra, H. Burchard, H. Ridderinkhof, H. E. De Swart, and M. J. F. Stive, Morphodynamics of the Wadden Sea and its barrier island system, *Ocean & coastal management*, *68*, 39–57, 2012.

A Appendix

A.1 Zeroth-order solutions

The ansatz for the solution of a simple harmonic oscillator is:

$$\hat{u}_0 = Ae^{ik_0x} + Be^{-ik_0x}.$$

The first boundary condition is:

$$\frac{\partial u_0}{\partial x} = \sin(t); \quad \text{at } \ x = 0.$$

Using Euler's formula, sin(t) can be rewritten:

$$\sin(t) = \frac{e^{it} - e^{-it}}{2i} = \Re\{ie^{-it}\}.$$

Recall that u_0 can be written as:

$$u_0 = \Re\{\hat{u}_0(x)\ e^{-it}\}.$$

Hence the first derivative with respect to x can be expressed as:

$$\frac{\partial u_0}{\partial x} = \Re\{\frac{d\hat{u}_0}{dx}\ e^{-it}\}.$$

So the boundary condition for the complex amplitudes becomes:

$$\frac{\partial \hat{u}_0}{\partial x} = i \quad \text{at } \ x = 0.$$

Applying this boundary condition leads to:

$$ik_0A - ik_0B = i,$$
$$(*) \quad A = \frac{1}{k_0} + B.$$

The second boundary condition is:

$$\hat{u}_0 = 0 \quad \text{at} \;\; x = \ell.$$

Applying it yields:

$$Ae^{ik_0\ell} + Be^{-ik_0\ell} = 0$$
$$(**) \quad A = -Be^{-2ik_0\ell}.$$

Combining (*) and (**) provides an expression for B:

$$\begin{aligned} B &= -\frac{1}{k_0(1+e^{-2ik_0\ell})} \\ &= -\frac{e^{ik_0\ell}}{k_0(e^{ik_0\ell}+e^{-ik_0\ell})} \\ &= -2\frac{e^{ik_0\ell}}{k_0\cos(k_0\ell)}. \end{aligned}$$

The expression for A then becomes

$$A = \frac{e^{-ik_0\ell}}{k_0\cos(k_0\ell)}.$$

Substituting the expressions for A and B in the ansatz, and some minor rewriting yields the final expression:

$$\hat{u}_0 = -i\frac{\sin(k_0(x-L_b))}{k_0\cos(k_0L_b)}.$$

From equation (17) it becomes clear that $\hat{\eta}_0$ is obtained by taking the derivative of u_0 to x and integrating it over t:

$$\hat{\eta}_0 = \frac{\cos(k_0(x-L_b))}{\cos(k_0L_b)}$$

A.2 First-order solutions

The first-order system is as following:

$$\frac{\partial u_1}{\partial t} + \frac{\partial \eta_1}{\partial x} + \lambda u_1 = -u_0\frac{\partial u_0}{\partial x} + \lambda u_0\eta_0,$$
$$\frac{\partial \eta_1}{\partial t} + \frac{\partial u_1}{\partial x} = -\frac{\partial}{\partial x}(u_0\eta_0),$$

with boundary conditions

$$\eta_1 = 0; \quad \text{at} \;\; x = 0,$$
$$u_1 = 0; \quad \text{at} \;\; x = \ell.$$

The following ansatzes are substituted into this system:

$$u_0 = \frac{1}{2}\hat{u}_{01}e^{-it} + \frac{1}{2}\hat{u}_{01}^{*}e^{it},$$

$$\eta_0 = \frac{1}{2}\hat{\eta}_{01}e^{-it} + \frac{1}{2}\hat{\eta}^*_{01}e^{it},$$
$$u_1 = \bar{u}_{10} + \frac{1}{2}\hat{u}_{12}e^{-2it} + \frac{1}{2}\hat{u}^*_{12}e^{2it},$$
$$\eta_1 = \bar{\eta}_{10} + \frac{1}{2}\hat{\eta}_{12}e^{-2it} + \frac{1}{2}\hat{\eta}^*_{12}e^{2it}.$$

Thereafter, the terms are seperated into two harmonics. The residual terms (no time dependence) and the overtide terms (e^{-2it}). Since the residual system was already fully solved in the main text, the focus will only lie on the overtide system. This becomes:

$$-i\hat{u}_{12} + \frac{1}{2}\frac{d\hat{\eta}_{12}}{dx} + \frac{1}{2}\lambda\hat{u}_{12} = -\frac{1}{4}\hat{u}_{01}\frac{d\hat{u}_{01}}{dx} + \frac{1}{4}\lambda\hat{u}_{01}\hat{\eta}_{01},$$
$$-i\hat{\eta}_{12} + \frac{1}{2}\frac{d\hat{u}_{12}}{dx} = -\frac{1}{4}\frac{d}{dx}(\hat{u}_{01}\hat{\eta}_{01}),$$

with boundary conditions

$$\hat{\eta}_{12} = 0; \quad \text{at } x = 0,$$
$$\hat{u}_{12} = 0; \quad \text{at } x = \ell.$$

The next step is solving the system per term (ADV,DDF,EMF). The method used in the following steps is the same for every independent term. Hence, only one will be given with a detailed calculation. In the case of just advection the system becomes:

$$(*) \quad -i\hat{u}_{12} + \frac{1}{2}\frac{d\hat{\eta}_{12}}{dx} + \frac{1}{2}\lambda\hat{u}_{12} = -\frac{1}{4}\hat{u}_{01}\frac{d\hat{u}_{01}}{dx},$$
$$(**) \quad -i\hat{\eta}_{12} + \frac{1}{2}\frac{d\hat{u}_{12}}{dx} = 0,$$

with the same boundary conditions as in the entire first-order system. Next, $\hat{\eta}_{12}$ is eliminated by substituting (*) into (**). The equations are also multiplied by $4i$ for convenience. This yields

$$\frac{d^2\hat{u}_{12}}{dx^2} + k_1^2\hat{u}_{12} = -i\hat{u}_{01}\frac{d\hat{u}_{01}}{dx},$$

with $k_1 = \sqrt{4 + 2i\lambda}$. Only the non-transient solution is of interest, for which the ansatz is

$$\hat{u}_{12} = A(x)\cos(k_1(x-\ell)) + B(x)\sin(k_1(x-\ell)).$$

The first derivative to x is

$$\frac{d\hat{u}_{12}}{dx} = -k_1A(x)\sin(k_1(x-\ell)) + k_1B(x)\cos(k_1(x-\ell)) + \cancelto{0}{\frac{dA}{dx}\cos(k_1(x-\ell)) + \frac{dB}{dx}\sin(k_1(x-\ell))}.$$

The last term dropping to zero is an educated guess, which will be verified when arriving at the expressions for $\frac{dA}{dx}$ and $\frac{dB}{dx}$. The second derivative is

$$\frac{d^2\hat{u}_{12}}{dx^2} = -k_1^2\hat{u}_{12} - k_1\frac{dA}{dx}\sin(k_1(x-\ell)) + k_1\frac{dB}{dx}\cos(k_1(x-\ell))$$

Substituting this into the differential equation leads to

$$-k_1 \frac{dA}{dx} \sin(k_1(x-\ell)) + k_1 \frac{dB}{dx} \cos(k_1(x-\ell)) = -i\hat{u}_{01} \frac{d\hat{u}_{01}}{dx}.$$

From this it follows that

$$\frac{dA}{dx} = \frac{i}{k_1} \sin(k_1(x-\ell)) \left(\hat{u}_{01} \frac{d\hat{u}_{01}}{dx} \right)$$

and

$$\frac{dB}{dx} = -\frac{i}{k_1} \cos(k_1(x-\ell)) \left(\hat{u}_{01} \frac{d\hat{u}_{01}}{dx} \right).$$

This confirms the 'educated guess'. The next step is to integrate one of these equations to x. For this, it is handy to find smart boundaries to integrate to. Substituting the ansatz for $\hat{u}_{12}$ into the boundary condition for for $\hat{u}_{12}$ at $x = \ell$ gives

$$A(\ell)\cos(k_1(\ell-\ell)) + B(\ell)\sin(k_1(\ell-\ell)) = 0,$$

$$A(\ell) = 0.$$

So the the integration will be from $x' = x$ to $x' = \ell$. This yields:

$$\int_\ell^x \frac{dA}{dx'} dx' = A(x) = \frac{i}{k_1} \int_\ell^x \sin(k_1(x'-\ell)) \left(\hat{u}_{01} \frac{d\hat{u}_{01}}{dx'} \right) dx'$$

To calculate sand transport only depends on the velocity at the entrance of the basin ($x = 0$), so all that is left to do is find an expression for $B(0)$. This can be done by using the boundary condition for $\hat{\eta}_{12}$ at $x = 0$ and equation (**). From this it follows that

$$\frac{d\hat{u}_{12}}{dx} = 0 \quad \text{at} \;\; x = 0.$$

Combining this reformulated boundary condition with the expression for $\frac{d\hat{u}_{12}}{dx}$ gives the following expression:

$$\begin{aligned} B(0) &= -A(0)\tan(k_1\ell), \\ &= -\left(\frac{i}{k_1} \int_\ell^0 \sin(k_1(x-\ell)) \left(\hat{u}_{01} \frac{d\hat{u}_{01}}{dx} \right) dx \right) \tan(k_1\ell). \end{aligned}$$

So the expression for $\hat{u}_{12}$ at $x = 0$ becomes:

$$\begin{aligned} \hat{u}_{12}(0) &= A(0)\cos(k_1(\ell)) - B(0)\sin(k_1(\ell)), \\ &= \left(\frac{i}{k_1} \int_\ell^0 \sin(k_1(x-\ell)) \left(\hat{u}_{01} \frac{d\hat{u}_{01}}{dx} \right) dx \right) \left(\cos(k_1\ell) + \frac{\sin^2(k_1\ell)}{\cos(k_1\ell)} \right), \\ &= \frac{i}{4k_1\cos^2(k_0\ell)} \left(\frac{\sin((k_1-2k_0)\ell)}{k_1-2k_0} - \frac{\sin((k_1+2k_0)\ell)}{k_1+2k_0} \right) \left(\cos(k_1\ell) + \frac{\sin^2(k_1\ell)}{\cos(k_1\ell)} \right). \end{aligned}$$

This calculation is repeated for depth-dependent friction, as well as divergence of excess mass flux.